Barbara Geier, BSc

Rapid and Highly Compact Purification at Room Temperature for Focused Electron Beam Induced Pt-C Deposits

MASTER THESIS

For obtaining the academic degree
Diplom-Ingenieur

Master Programme of
Technical Physics

Graz University of Technology

Supervisor:

Ao.-Univ.-Prof. Dipl.-Ing. Dr. techn. Werner Grogger

Institute for Electron Microscopy and Nanoanalysis

Co-Supervisor:

Dipl.-Ing. Dr. techn. Harald Plank

Graz, June 2014

Abstract

Focused electron beam induced deposition (FEBID) is a versatile direct write method for the fabrication of functional 3D structures with spatial nanometer resolution. Since the beginning, the massive carbon incorporation up to 90 at.% was a major issue as this reduces or even masks the intended functionalities.

In this thesis we demonstrate a simple approach for the entire carbon removal in FEBID (nano)structures grown by MeCpPt^{IV}Me$_3$ precursor. The purification process consists of an electron-beam assisted post-growth treatment in combination with H$_2$O vapour at room temperature performed in an environmental scanning electron microscope. This approach eliminates the necessity of using complicated gas delivery systems, highly reactive gases and sample/gas heating systems which were often needed in the past. As will be shown, this strategy enables fast carbon removal at rates better than 5 min.nA^{-1}.µm^{-2} and also provides pore and crack free deposits while original footprints and 3D surface features are maintained. Finally, the deposit dimensionality is systematically reduced from 3D to quasi-1D to demonstrate the applicability of the introduced process. The study is complemented by a detailed discussion of the purification mechanism including theoretical calculations and Monte Carlo simulations. Hence, this thesis ranges from a concept and its detailed experimental studies to fundamental insights in the process itself. The main outcome of this thesis, however, is the introduction of the first purification process for platinum based FEBID structures at room temperature which entirely removes the unwanted carbon without affecting the original morphology.

Kurzfassung

Fokussierte Elektronenstrahl induzierte Abscheidung (focused electron beam induced deposition, FEBID) ist eine vielseitige, direkte Schreibmethode zur Erzeugung von Nanostrukturen. Schon von Anfang an war der Einbau von Kohlenstoff in die Nanostrukturen, welcher bis zu 90 at.% betragen kann ein großes Problem, da dadurch die beabsichtigten Funktionalitäten reduziert oder gar unterdrückt werden.

Diese Diplomarbeit demonstriert eine einfache Methode, um den Kohlenstoff aus FEBID Abscheidungen, welche mittels MeCpPt^{IV}Me$_3$-Precursor hergestellt wurden, vollständig zu entfernen. Bei diesem Prozess werden die Nanostrukturen durch ein Environmental Scanning Electron Microscope in Wasserdampf-Umgebung mittels eines rasternden Elektronenstrahls bei Raumtemperatur aufgereinigt. Der Vorteil dieser Methode ist, dass hierfür keine Gaszufuhrsysteme, reaktive Gase oder Proben bzw. Gas-Heizsysteme benötigt werden. Es wird gezeigt, dass diese Vorgehensweise den Kohlenstoff mit Raten schneller als 5 min.nA^{-1}µm^{-1} beseitigt. Hervorzuheben ist, dass durch diesen Prozess poren- und bruchfreie Strukturen entstehen, während der ursprüngliche Grundriss und 3D-Oberflächen-Strukturen erhalten bleiben. Zusätzlich wurde die Dimension der Abscheidung systematisch von 3D zu quasi-1D reduziert, um die Anwendbarkeit des eingeführten Prozesses zu zeigen. Eine detaillierte Diskussion des Aufreinigungsmechanismus samt theoretischer Berechnungen und Monte Carlo Simulationen wird dargestellt. Diese Diplomarbeit spannt den Bogen vom Konzept über detaillierte experimentelle Untersuchungen bis hin zu grundlegenden Einblicken in den Prozess selbst. Das Resultat dieser Arbeit ist die Einführung des ersten Aufreinigungsprozesses für Platin basierte FEBID Strukturen bei Raumtemperatur, der den ungewünschten Kohlenstoff komplett entfernt ohne dabei die ursprüngliche Morphologie zu beeinflussen.

Acknowledgements

First of all I would like to thank the head of the institute, Prof. Ferdinand Hofer, for giving me the opportunity to write my master thesis at this institute.

I also owe gratitude to Prof. Werner Grogger for being my supervisor and for his cooperation.

Especially, I would like to thank Dr. Harald Plank, for his incredible support, his encouragement and trust. I want to express my appreciation to him for teaching me, for taking his time and for caring.

I would also like to thank DI Roland Schmied, DI Robert Winkler and Dr Johannes Rattenberger for their constant advice.

My gratitude also goes to DI Angelina Orthacker and Dr Christian Gspan for performing the TEM investigations. Also, I would like to thank the entire FELMI staff members for their advice and help throughout my thesis.

My thanks also go to the colleagues and friends at the institute for spending some good times.

This thesis is the result of an 18 year-long education and would not have been possible without the constant help and support from my family and friends. Most of all I would like to thank my parents for their unquestioning love, encouragement and support. I also owe gratitude to my three brothers who prepared me for life and always supported me when needed. I also want to express my gratitude to all my friends and especially to my boyfriend Robert, who were my personal and mental backups during my studies.

Table of Contents

List of abbreviations

AFM	...	*atomic force microscope*	GIS	...	*gas injection system*
BSE	...	*back scattered electrons*	HAADF	...	*high angle annular dark field*
DBM	...	*dual beam microscope*	HR-TEM	...	*high resolution TEM*
DEA	...	*dissociation electron attachment*	HV	...	*high vacuum*
DI	...	*dissociation ionisation*	LIMS	...	*liquid ion metal source*
DT	...	*dwell time*	LJ	...	*Lennard Jones*
EC1	...	*first environmental chamber*	MCA	...	*multi-channel analyzer*
EC2	...	*second environmental chamber*	MLR	...	*mass transport limited*
ED	...	*environmental distance*	PE	...	*primary electrons*
EDXS	...	*Energy dispersive x-ray spectrometer*	PoP	...	*point pitch*
ELR	...	*Electron limited regime*	PSD	...	*position sensitive detector*
ESEM	...	*Environmental scanning electron microscope*	RT	...	*refresh time*
EDXS	...	*Energy dispersive x-ray spectrometer*	SE	...	*secondary electrons*
EELS	...	*electron energy loss spectroscopy*	SEM	...	*scanning electron microscopy*
FEBID	...	*focused electron beam induced deposition*	SDR	...	*surface diffusion replenishment*
FEG	...	*field emission gun*	STEM	...	*scanning transmission electron microscopy*
FIB	...	*focused ion beam*	SGT	...	*stagnation gas thickness*
FIBID	...	*Focused ion beam induced deposition*	TEM	...	*transmission electron microscopy*
FSE	...	*forward scattered electrons*	UHV	...	*ultra high vacuum*
FWHM	...	*full width at half maximum*	VdW	...	*Van der Waals*

1 Introduction and Motivation

During the last decade, focused electron beam induced deposition (**FEBID**) has attracted increasing interest as direct write method for the fabrication of even complex and free-standing 3D structures with spatial resolutions in the sub-10 nm range.[1] FEBID bases on functional precursor molecules which are injected into a scanning electron / scanning ion / dual beam microscope chamber in close proximity of the substrate. After physisorption, the molecules randomly diffuse and desorb again after an intrinsic residence time. If the electron beam and its subsequently re-emitted electrons interact with the precursor molecules during the diffusion period they get dissociated into volatile and non-volatile parts. While the former gets pumped away the latter remains on the surface as functional (nano)deposit.

Depending on the precursor chemistry, a variety of different functionalities, ranging from conductive, semi-conductive, insulating and magnetic material properties can be obtained. The major advantage of this method is the maskless character with the possibility to write on even non-flat surfaces with no need of special sample preparation prior or after fabrication. Hence, this method represents a very powerful tool for rapid prototyping ranging from optical[2], mechanical or gas sensing[3] applications.

In early years FEBID had a bad reputation as it was known as a slow process, prone to unwanted proximity deposition due to the complex electron trajectories in solids and the significant impurity level by carbon which reduced or even masked the intended functionality. While significant progress has been made with respect to the two former aspects[3-13] the latter remained, as e.g. for $MeCpPt^{IV}Me_3$ precursor the incorporated carbon leads to electric resistivities about 6 - 8 orders of magnitudes higher than of pure platinum[14,15]. Hence, a lot of attention has been put on *in-* and *ex-situ* purification methods such as synchronized laser assisted FEBID[16,17], post-growth annealing [18,19-21], co-deposition with reactive gases during fabrication[22], *in-* and *ex-situ* temperature treatments[5,19,20,23-25] and others comprehensively summarized by Botman et al.[26].

Recently, Mehendale et-al.[21] demonstrated the entire carbon removal from $MeCpPt^{IV}Me_3$ based FEBID deposits by an e-beam assisted post-growth-treatment using oxygen gas at elevated temperatures of 120°C. Although excellent in purity, the structures suffered from severe porosity and cracks, putting nanoscale applications in question. The used approach led to purification rates of ~144 $min.nA^{-1}.\mu m^{-2}$ at a primary electron energies of 5 keV performed on sub-100 nm deposits. Slightly later, Plank et al.[7] revealed the local gas pressure and the gas temperature as decisive elements with respect to efficiencies and carbon free, high fidelity surface morphologies, respectively. While purification rates better than 10 $min.nA^{-1}.\mu m^{-2}$ were achieved, a small lateral shrink of the deposits remained together with slightly increased gas temperatures of 50°C due to technical limitations at that time.

In this thesis we push the concept by Plank et-al even further and introduce an even simpler post growth purification process by an e-beam assisted approach using H_2O vapour at room temperatures. As we will show, this strategy allows full purification at rates better than 5 $min.nA^{-1}.\mu m^{-2}$ while the original footprint shapes are maintained with minimal lateral shrinking. Furthermore, we demonstrate the purification of quasi-2D single lines and quasi-1D nanopillars, all exhibiting pore free, high fidelity shapes. Finally, the study is complemented by a fundamental insight in the purification mechanism.

2 Instrumentation

2.1 Dual Beam Microscope

A Dual Beam Microscope (**DBM**) combines a scanning electron microscope (**SEM**) and a focused ion beam (**FIB**) microscope. The advantage is the possibility of simultaneous imaging with the SEM during e.g. a sputtering process operated by the FIB.

The possibility of positioning the ion beam, which can have a diameter as small as 5 nm, is very accurate and with the ability to control exposure times, known as dwell times (**DT**), gives the opportunity to use this microscope as *a* nanoscalpel. Subsequently, surfaces can be structured rapidly and accurately which is a big advantage for the rapid prototype development.

Most frequently the DBM is used to prepare thin lamellas (<50 nm) from a selected area of a specimen for transmission electron microscopy (**TEM**) investigations. For this application it is necessary to have gas injection systems (**GIS**) to deposit a protective layer and to mount the lamella on the micromanipulator in order to transfer it to the TEM grid and to glue it on.

Another application of the DBM in combination with the GIS system is the deposition of nanostructures. Precursor material gets chemically separated by the electron/ion beam, due to the particle interaction into a volatile and non-volatile part. The volatile part gets pumped up and the non-volatile part condenses. When the precursor material gets separated by the ion beam we talk about Focused Ion Beam Induced Deposition (**FIBID**) and by electron beam it is called Focused Electron Beam Induced Deposition (**FEBID**). Figure 1 shows the DBM FEI NOVA 200 which was used for the thesis.
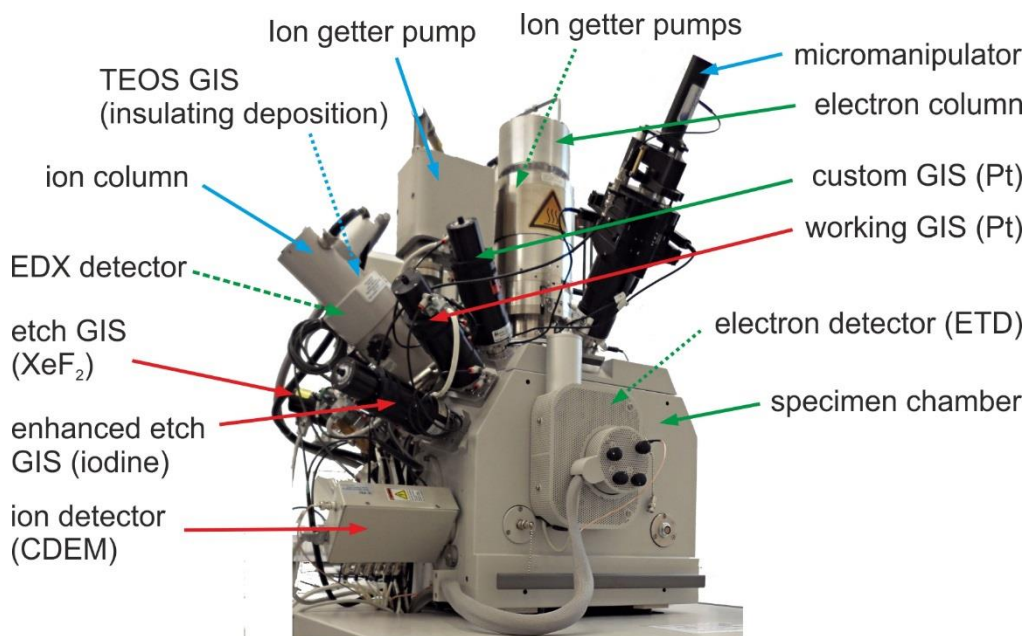

Figure 1: FEI NOVA 200 dual beam microscope. The green and blue arrows indicate the parts which were used for this thesis. The blue arrows show the parts which were only used for the preparation of the TEM lamella. The dashed arrow lines specify the parts which are not visible in this picture.[27]

The ion and electron beam include an angle of 52°. They cross at a certain point which is indicated as eucentric height. In order to work with both beams in focus we have to move the stage to the eucentric height which is at our microscope at ~5 nm below the last lens of the electron column. A smaller eucentric height would be favourable for the resolution; however, it also has to be considered that space between the specimen and electron column is needed for the GIS, micromanipulator and detectors.[1]

2.1.1 Vacuum System

High vacuum (**HV**) in the chamber is necessary to avoid scattering of electrons at the gas atoms.[28] The chamber vacuum is generated by using roughing pumps and subsequently supported by a turbomolecular pump when a certain pressure is reached. Electron source and ion source need to be in ultra-high vacuum (**UHV**) which is reached by using ion getter pumps, as can be seen in Figure 1.

2.1.2 Electron Column

The electron column of the dual beam microscope is equipped with a Schottky emitter which needs to be operated in UHV. The electron emission takes place in a fine, heated tungsten tip covered ZrO_2 in order to reduce the work function barrier, placed in a strong electric field which lets the electrons tunnel through a strongly curved tip. A special construction, denoted as Wehnelt Cylinder, bundles the electrons in the so called first cross over.[28]

Afterwards, the electrons get accelerated further and are led into two electromagnetic condenser lens systems which demagnify the beam and align it parallel on the optical axis (C1,C2 Figure 2).
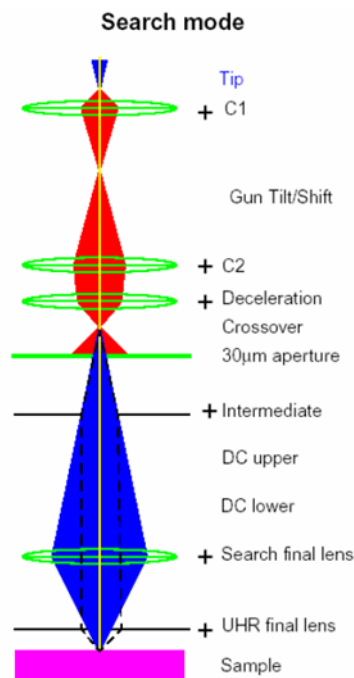

Figure 2: schematic illustration of the SEM lens system in the used dual beam microscope.[29]

The lens system is also used to control the current by taking different areas of the first crossover. Afterwards, the electron energy gets reduced to the desired value (0.5-30 keV) and they are directed through an aperture. Duplex lens system is used to guide the beam in X- and Y-direction. The axial astigmatism gets corrected by this lens system. Finally, the electrons pass through the objective lens to focus the beam on the sample.

Magnetic lenses are used in electron and ion column to reduce the source diameter. The big advantage is that the strength of magnetic lenses can be adjusted continuously by changing the current through the coil, in contrast to optical lenses. The resolution is not limited by the wavelength; however, it is determined by lens aberrations. The aberrations with the biggest impact are: spherical aberration, chromatic aberration, diffraction error and axial astigmatism.[28]
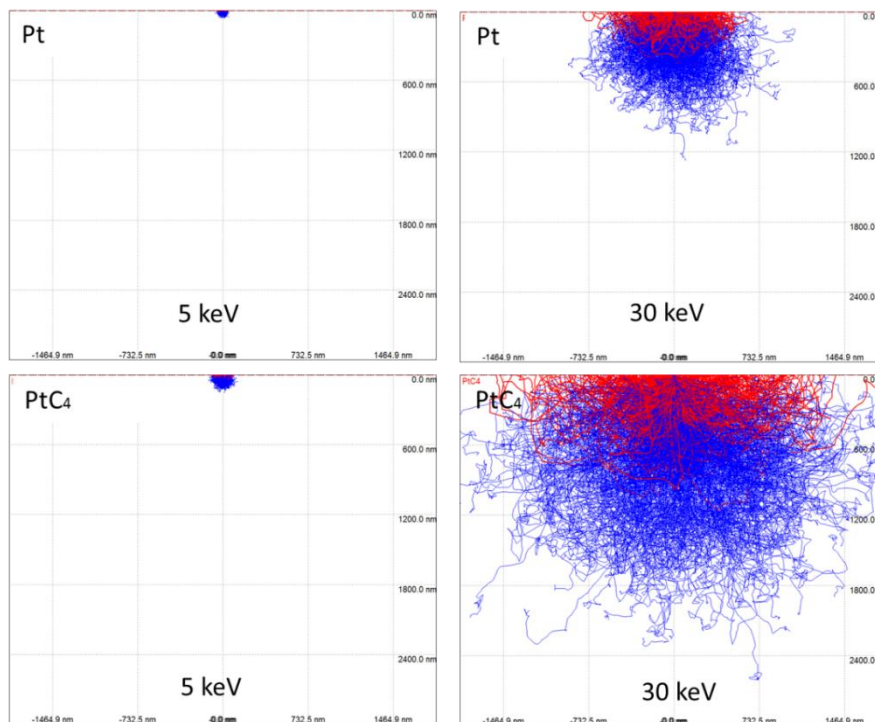
Figure 3: in-scale CASINO[30] simulations of electron trajectories for Pt (top) and PtC$_4$ (bottom) for different primary electron energies of 5 keV (left) and 30 keV (right) in order to visualize the influence of primary beam energy and density of the sample on the penetration depth. BSE electrons are displayed in red and electrons which finally lost all their energy in the bulk are indicated in blue.

2.1.3 Interaction of Electrons with Matter

When primary electrons (**PE**) enter the sample there are several possible ways of interaction: electrons that are scattered elastically and leave the surface in great angle are called backscattered electrons (**BSE**). Inelastically scattered electrons lose small parts of their energy and are deflected in small angles until they are stopped. The depth of interaction depends on the primary energy of electrons and on the atomic number of the material of the sample (see Figure 3). PE and BSE can lose their energy by striking electrons out of their atomic shell which are denoted as secondary electrons (**SE**). When SEs are generated by

PEs they are indicated as SE_1, from BSE as SE_2 and from forward scattered electrons (**FSE**) as SE_3. SEs can only leave the sample (and are detectable) when they were generated close to the surface of the sample (<10 nm), due to the small energy (<50 eV) of the SEs (see Figure 4). Due to this fact the best resolution is given for SEs which originate from PE and this signal is mainly used for imaging. BSEs give qualitative information about the atomic number of certain areas of the sample. Characteristic X-rays are generated when an inner shell atom is knocked out, which is explained in detail in section 2.2.3.
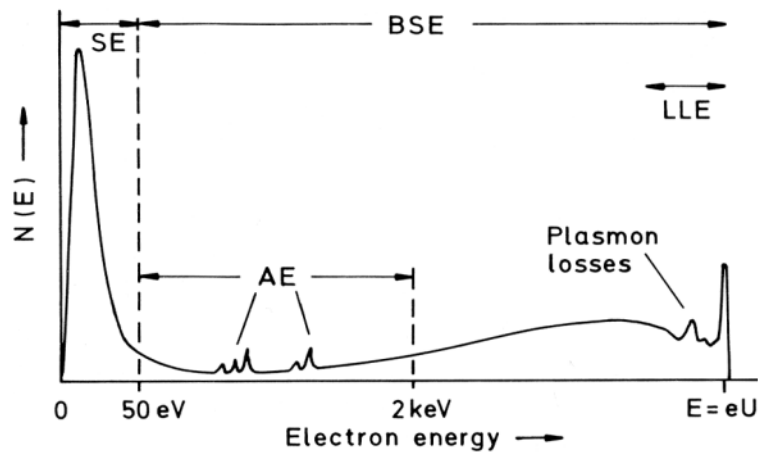

Figure 4: energy distribution of detectable electrons. SEs are low energy electrons (<50 eV), Auger electrons (AE) have element specific energies in the range of 50 eV to 2 keV, low loss electrons (LLE) are BSEs which only lose small fractions of their energy. [31]

2.1.4 Ion Column

Most FIB microscopes use Ga^+ ions for the liquid ion metal source (**LIMS**), due to the low melting point (easy liquefaction), low vapor pressure (low unwanted losses and so a longer durableness) and it is also not miscible with tungsten (tip-material).

The Ga^+ ions are produced by a liquid source. A reservoir, which is filled with gallium, gets heated above the melting point of gallium, which is at 29.8°C. The gallium coats in liquid conditions a tungsten hairpin which is placed at the bottom of the reservoir, due to gravity and forms a droplet on the tip. Through an extractor, which is set on a very high potential and has field intensities higher than 10^8 V.cm^{-1}, the droplet gets deformed to a so called Taylor cone. Due to the strong curvature of the droplet the electric field becomes very high and because of the ability of gallium to lose valence electrons fairly easy, an intense localized Ga^+ beam is generated. The beam gets directed through the so called beam acceptance aperture which is placed above the condenser lens system to parallelize the beam (Figure 5). Next, the beam defining aperture limits the ion current (1-20 000 pA) and beneath the beam blanker is used to screen off the destructive ion beam when it is not needed. The subjacent octopole coils are used to lead the beam over the surface and for correcting the astigmatism. The last lens (objective lens) focusses the ion beam on the sample.
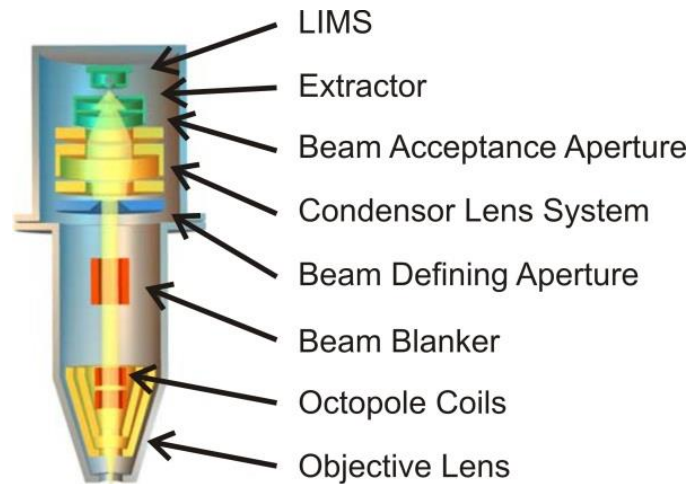
Figure 5: schematic illustration of the ion column for the used dual beam microscope.[32]

2.1.5 Interaction of Ions with Matter

Focused electron beams practically do not lead to removal of material through momentum transfer, however, focused ion beams cannot be lead over the surface without causing a damage which is known as sputtering. Sputtering is the main interaction mechanism for FIB processes. Beside the emission of atoms, ions and clusters, a big amount of SEs are generated which is responsible for imaging.

As Ga^+ ions are much bigger in comparison to electrons, they collide with atoms and molecules, leading due to the high electron energy to a destruction of the sample material. The ion loses its energy by collision and changes its direction. According to the size of the ions and for an acceleration energy of 30 keV Ga^+ ions typically penetrate 5-70 nm into the sample depending on the density of the sample. This leads to a permanent implementation of ions in the solid.

Atoms, ions or clusters which are knocked out of their position can activate following processes depending on their energy: phonons get excited leading to a significant rise in temperature. In neighboring areas valence electrons can be released and a big amount of secondary electrons are generated. Additional displacement processes can be activated leading to amorphization of the interaction volume or an emission of ions, atoms and clusters including emission of secondary-ions and -atoms. The latter two processes are mainly responsible for the sputtering process which is supported by thermally induced evaporation in the proximity of the ion beam. The sputter rate depends on the material (bonding energies) as well as on the relative orientation of the crystals (for crystalline material).

2.2 Environmental Scanning Electron Microscope

Environmental Scanning Electron Microscopes (**ESEM**) are used to investigate e.g. biological tissue, samples that are damp or wet, porous samples as bones, liquids in their original state due to the fact that the pressure in the sample chamber can be in the kPa range. The presence of the above mentioned samples would either contaminate the vacuum chamber or they are unsuited for vacuum environment.[28]

ESEMs can operate while the chamber contains a gas or vapor at a pressure between 10-2700 Pa due to a differential pumping system. The gaseous atmosphere allows insulating or poorly conducting samples to be investigated in stable manner without prior coating with a contacting layer.[28]

ESEMs are constructed in the same way as SEMs, however additions to the vacuum systems are included. The vacuum system is divided into five stages in order to decrease the pressure by pressure limiting apertures. Figure 6 is a schematic illustration of the stages, which are the sample chamber, first environmental chamber (**EC1**), second environmental chamber (**EC2**), column and gun.[33]
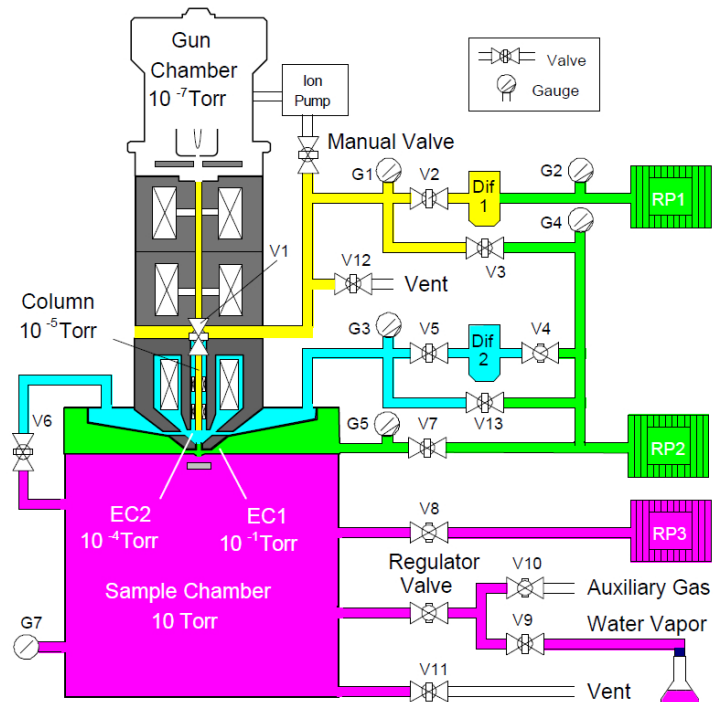
Figure 6: schematic illustration of the 5 stage pumping system in an ESEM which are the sample chamber, first environmental chamber (EC1), second environmental chamber (EC2), column and gun.[33]

The most important part are the two pressure limiting apertures placed at the bottom of the pole piece which separates the sample chamber (purple) from the EC1 (green) and EC2 (blue) in order to receive a pressure gradient as schematically illustrated in Figure 7. The diameter of the apertures is usually a few hundred micrometers, following an allowed pressure differential of a factor 100-1000 is achieved between the column and the specimen chamber.[28] The ESEM FEI Quanta 200 equipped with a tungsten cathode was used for the purification process due to the ability of spatially homogeneous, stable and controllable H_2O vapour atmospheres.

Figure 7: enlarged schematic drawing of the two pressure limiting apertures (PLA1, PLA2) placed in the final lens assembly allowing a pressure up to 50 Torr in the specimen chamber by remaining HV conditions in the gun.[33]

2.2.1   Environmental Secondary Electron Detection

For imaging in an ESEM SEs are taken as well because they provide the highest resolution images. An environmental secondary d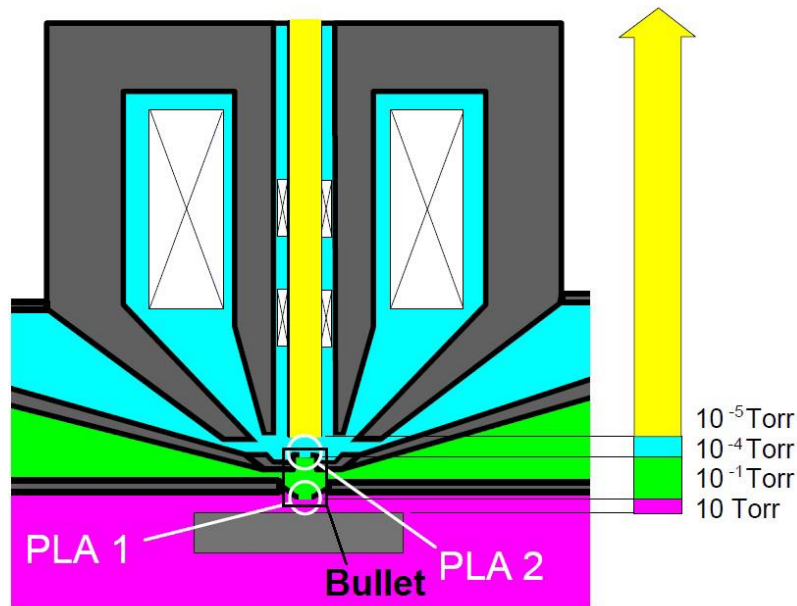etector (**ESD**) consists of an electrode placed concentrically at the bottom of the pole piece as schematically illustrated in Figure 8. SEs are attracted to the detector by the applied positive potential of a few hundred volts. Due to the gaseous ambient in the specimen chamber the SE signal gets amplified as electrons collide with the gas molecules. Hence, gas molecules get ionized resulting in the creation of additional electrons, denoted as environmental secondary electrons. The ionization process repeats many time leading to a proportional cascade amplification of the primary SEs signal which is collected by the detector. Additionally, the generated positive ions are attracted to the specimen surface as electrons accumulate from the e-beam which supress charging artifacts.[33]

2.2.2   Current Measurements in ESEM

In order to investigate the scattering cross section of electrons in the H_2O vapor of 10 Pa and 100 Pa a Faraday Cup was used. In ESEM mode the e-beam scatters due to interaction with H_2O vapor occurring mainly in small angles[34]. Therefore, the acceptance angle of the measuring device is one of the most important parameters. Current measurements in HV can be conducted by using a simple Faraday Cup which would also measure electrons which hit the device in the proximity of the aperture. However, in ESEM mode there is a big amount of positive gas ions, as the SE signal can be amplified several hundred times[35] and a lot of ions recombine at the cup. Subsequently, the positive specimen current would interfere with the

measurement of the electron beam current when the Faraday Cup is not modified in order to shield the positive current.
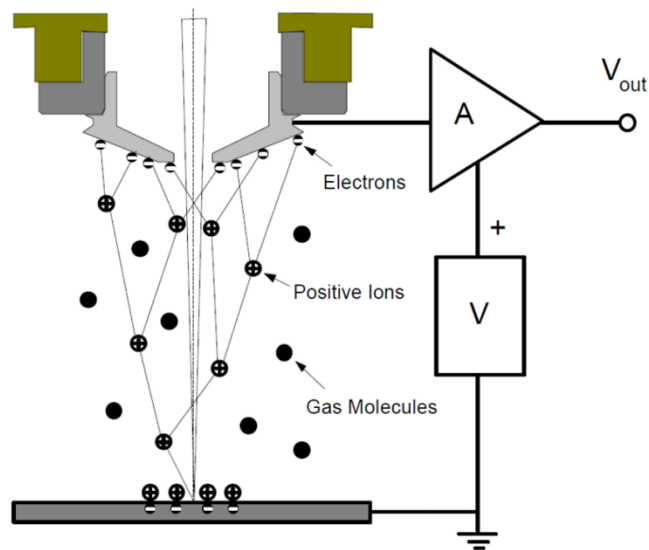
Figure 8: ESD detector uses gas ionization in order to amplify the SE signal. In isolating samples the positive ions are attracted to the surface of the specimen as electrons accumulate from the e-beam. [33]

Hence, a new Faraday Cup was developed by the design of Flechter et.al.[36] which was the main topic of the Master Thesis by Harald Fitzek[37]. Figure 9 shows the schematic drawing of the used Faraday Cup. The 10 µm aluminum aperture on top is grounded and isolated to the remaining cup by using a double cello tape with ~3 mm hole in the middle (isolator). Hence, the scattered electrons and the ions which are generated by the SE-detector are adsorbed. Unscattered electrons pass through both apertures and are detected by the Faraday Cup.[37]

Figure 9: schematic illustration of the Faraday Cup.[38]

However, it has to be considered that electrons which are scattered in a radius of 5 µm around the not scattered beam radius will be still detected. Subsequently, the current will always be measured too high.[37]

2.2.3 Energy Dispersive X-Ray Spectrometer

The ESEM is also equipped with an Energy Dispersive X-Ray Spectrometer (**EDXS**). X-rays are generated by the interaction of primary electrons with core electrons creating the characteristic X-rays or by inelastic scattering which leads to the Bremsstrahlung, as illustrated in Figure 10.
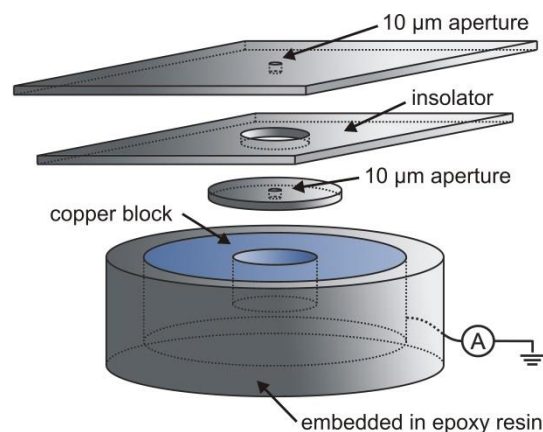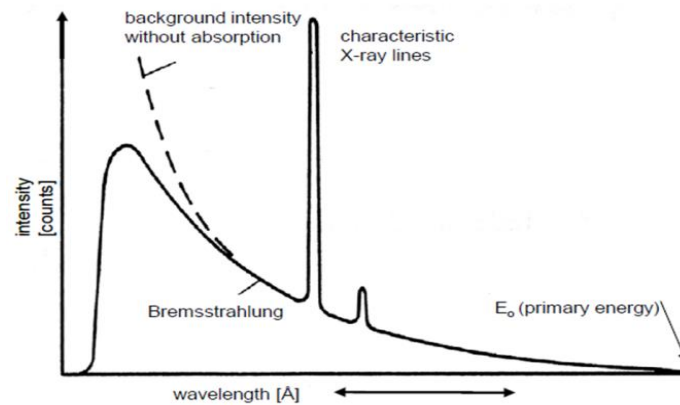

Figure 10: schematic illustration of an EDXS signal containing Bremsstrahlung and characteristic x-ray lines. [31]

The primary process of X-ray generation gets started by incoming electrons which knock out core electrons of the atoms. The generated core hole will be filled by an electron from a higher energy level which leads to an energy difference. On the one hand the energy difference will be released by either emitting a characteristic X-ray photon or on the other hand by direct transition to an electron from a lower energy shell which will leave the atom with some remaining kinetic energy, known as Auger electron. X-rays can be classified in series according to the shells where the ionization took place (K, L, …) and on the second position a Greek letter with a number as subscript indicates the shell of the core hole filling electron. For example $K\alpha_1$ stands for an ionization process which took place in the K shell and the accrued hole was filled by an electron from the $L_3(2P_{3/2})$ shell. Some possible transitions are forbidden due to selection rules.

Intensities of X-ray lines also depend on the ionization cross section and on the ionization probability which is known as fluorescence yield. The complementary fluorescence yield is known as Auger yield which indicates the probability of a radiation less transition. For low atomic number Z the probability of X-ray emission is very low, as can be seen in Figure 11.

The width of X-ray peaks ΔE is related to the life time of the energy state by Heisenbergs uncertainty relation: $\tau \Delta E \geq \hbar/2$. Following that, the lifetime τ of the state is inversely proportional to ΔE. However, the energy resolution of e.g. Si(Li) detectors (>100 eV) is certainly larger than the natural line width.

There are three different interaction mechanisms of x-rays with matter contributing to X-ray adsorption: elastic scattering, inelastic scattering and photoelectric adsorption. For quantitative analysis X-ray adsorption has to be considered.
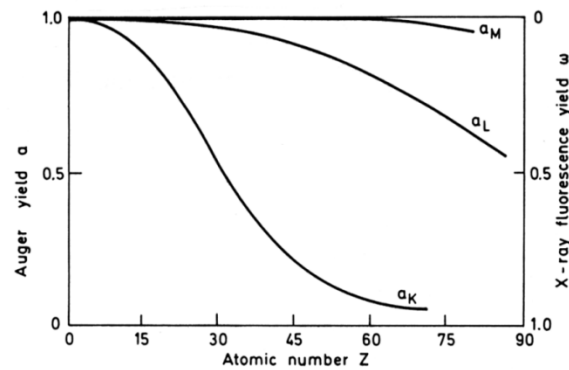
Figure 11: auger yield in dependency of the atomic number Z.[31]

The three main parts of an energy-dispersive X-ray spectrometer (**EDXS**) are the detector, the processing electronics and multi-channel-analyzer (**MCA**) display. The incoming x-rays generate electron-hole pairs in the semiconductor detector (either Si(Li) or HPGe). To transfer an electron from the valence to the conduction band an energy of 3.8 eV is required for silicon. X-rays typically have energies higher than 1 keV, hence thousands of electron hole pairs are generated by the income of a single X-ray photon. The number of the generated electrons and holes is directly proportional to the X-ray energy. Electron and holes get separated by a bias of a narrow p-n junction. So the detector generates a charge pulse due to the applied high voltage. Next, the signal is amplified by a field effect transistor and then identified electronically. The MCA stores the digitized signal in a channel assigned to that energy.[28]

Figure 12: schematic illustration of an energy dispersive X-ray spectrometer (EDXS)[39]

The EDXS system of our FEI NOVA 200 DBM is equipped with a silicon drift detector (**SDD**) which excels in the better count rate capability and energy resolution compared to the Si(Li) detector installed on the ESEM. The SDD detector was only used for recording final EDXS spectra.

2.3 Atomic Force Microscopy (AFM)

2.3.1 Concept

With an atomic force microscope (**AFM**) it is possible to investigate the morphology of a sample with a resolution in the sub-nanometer range. The big advantag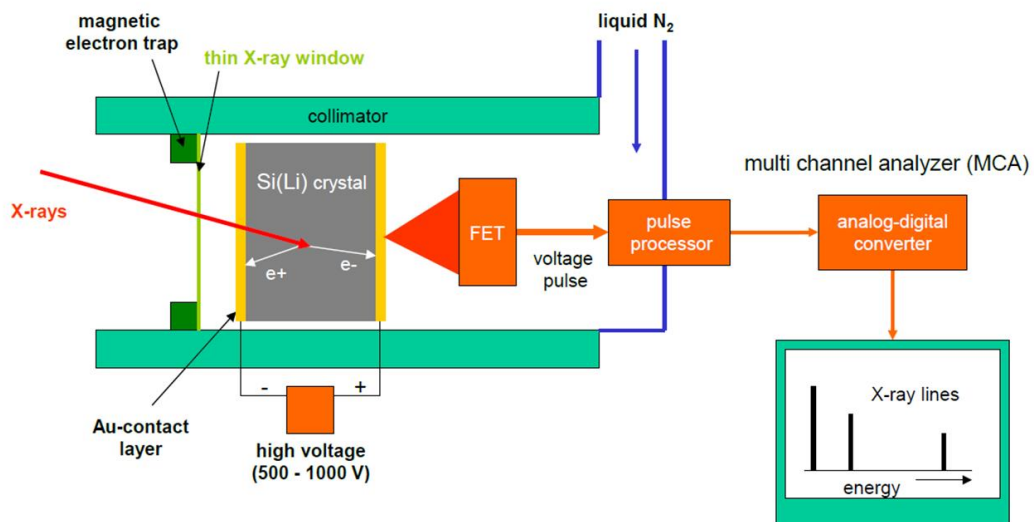e of this method is the possibility to obtain a 3-dimensional image of the surface morphology and the more or less non-destructive examination of the sample.
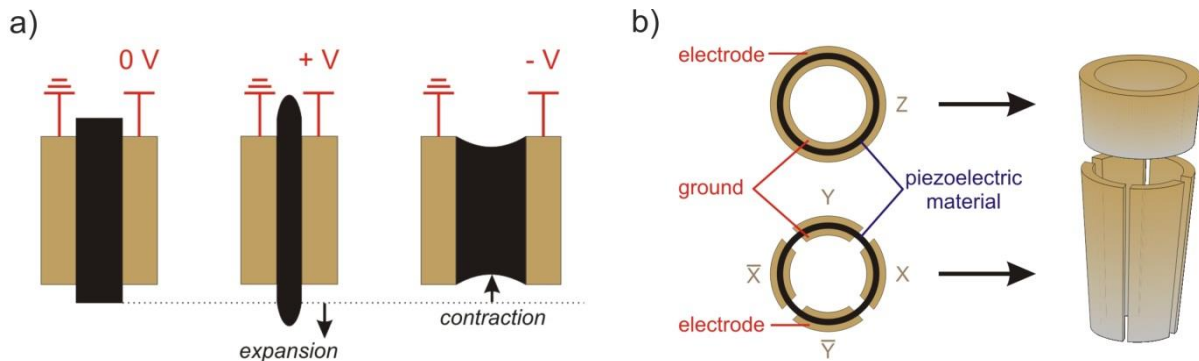
Figure 13: schematic illustration of the AFM motion system.[32]

Basically, a fine tip is mounted on a soft cantilever which is guided on the surface and the deflection of the cantilever gets detected with an optical system. The motion system is realised with piezoelectric crystals guiding the cantilever over the sample up to the pico-meter range. An applied voltage leads to a contraction or expansion of the crystal, as illustrated in Figure 13a. In order to achieve motions in all three spatial directions, a so called tube scanner is used, as can be seen in Figure 13b. Applying a positive voltage on one side of the electrode and a negative on the other side leads to a contraction on one radial segment and an expansion on the opposite segment, so the cantilever gets shifted. For guiding the cantilever in the vertical direction the topmost ring is used.
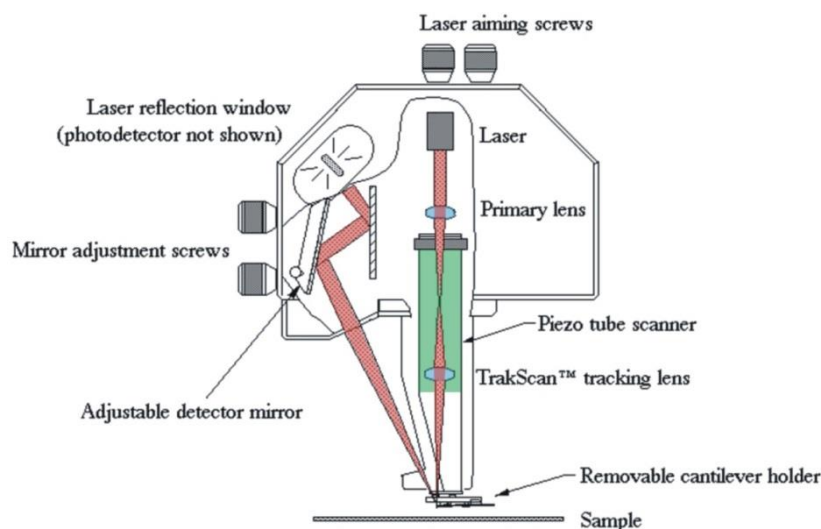
Figure 14: schematic illustration of the scanhead of the used AFM[32]

2.3.2 Detection System

Figure 14 illustrates the scan-head of the used microscope which can be considered as the most significant part of an AFM. The laser is focused on the foremost part of the cantilever and gets reflected to the adjustable mirrors and finally to the position sensitive detector (**PSD**).

When a force is applied on the tip, the cantilever deflects and the reflected laser dot changes its position on the PSD as shown in Figure 15. Subsequently, it is possible to detect vertical deformations of the cantilever and draw conclusions on the shape of the inspected nanostructure.
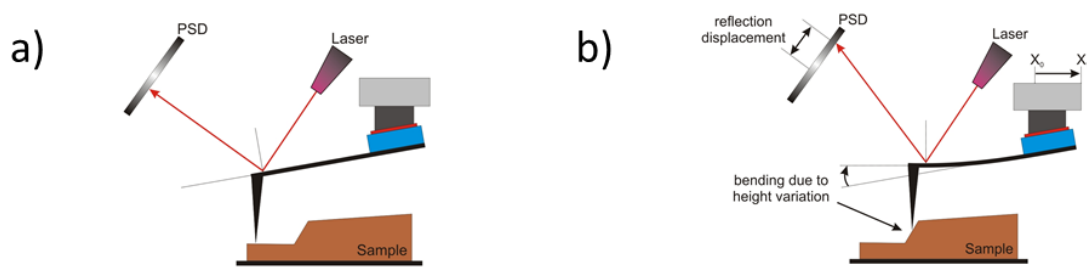
Figure 15: detection system of an AFM. By alteration of the surface structure from the original state (a) the cantilever gets deflected, subsequently the reflected laser spot on the PSD changes its position (b).[32]

To resolve surface structures very accurately, tips with a fine opening angle are beneficial. Normally, tips have a radius of ~10-20 nm in the front, as can be seen in Figure 16. It has to be considered that the detected signal is a convolution of the tip geometry and the specimen surface. A convolution leads to a broadening of the structures, to adulterated edges and the lateral resolution is limited as can be seen in Figure 17. The opening angle of the tip has a significant impact for very steep edges as can be seen in Figure 17a/b and also tip impurities have an effect on convolution (Figure 17c).
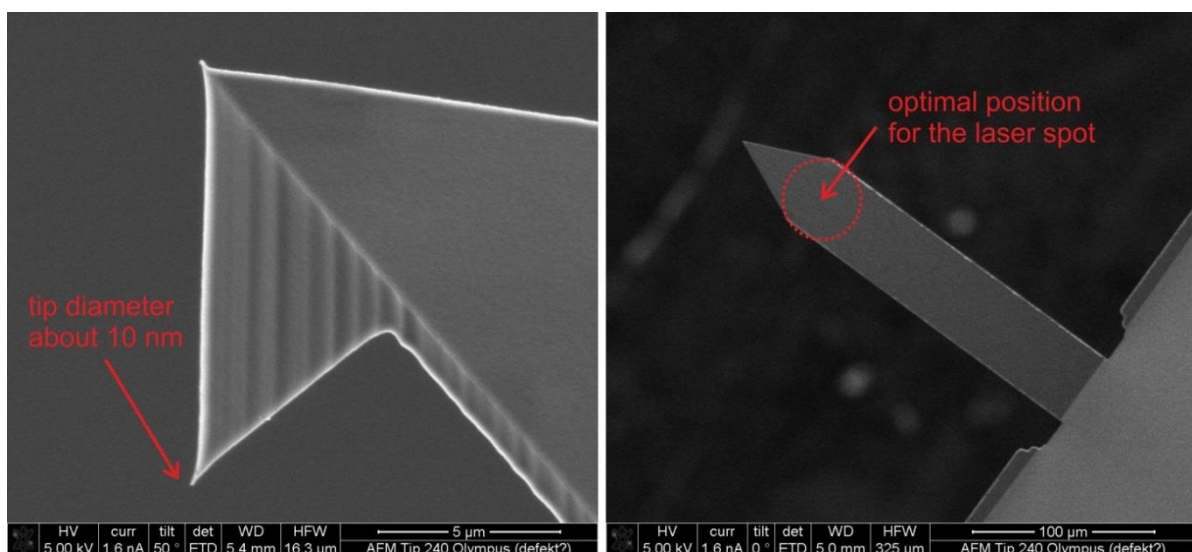
Figure 16: SEM image of the AFM tip and cantilever [32]
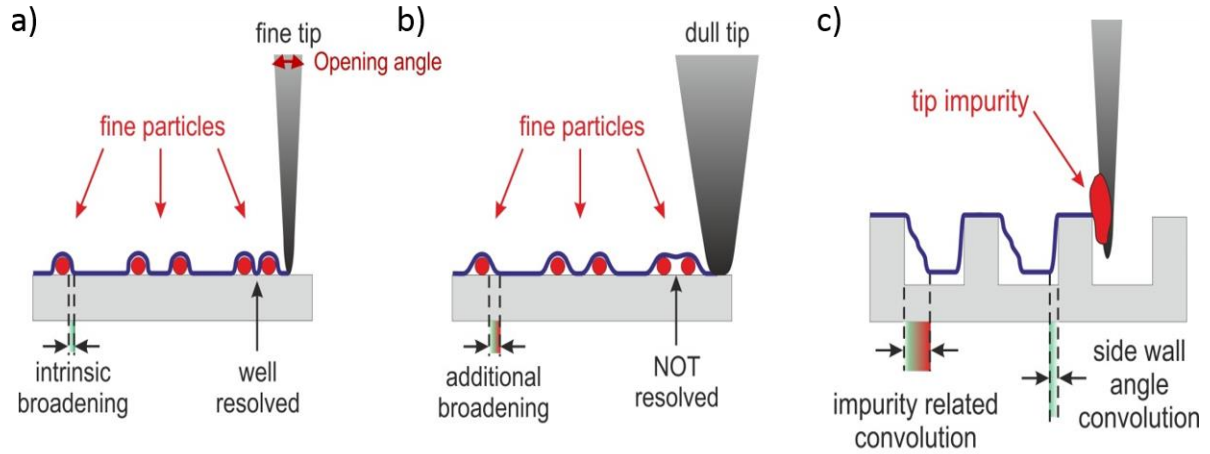
Figure 17: schematic illustration of the influence of the AFM tip radius on imaging of fine structures.(a,b) and in c) the impact of the opening angle on the measurement of a steep flank (on the right side) and impurity related convolution (on the left side).[32]

2.3.3 Forces

When the tip approaches the surface different forces are effective:

- Electrostatic (magnetic) forces for distances between tip and surface greater than 10 nm
- Van der Waals (**VdW**) forces for distances of ~10 nm till 5 nm
- Electron-electron repulsion (Pauli exclusion principle) is effective for distances smaller than ~2 nm

Typically, the tip is located at distances smaller than 10 nm for AFM images. Subsequently, only VdW forces and electron-electron repulsion has to be considered. Hence, the Lennard Jones (**LJ**) potential can be used to describe the interaction potential:

$$V_{LJ} = -V_{rep} + V_{VdW} = \frac{b}{r^{12}} - \frac{a}{r^6}$$

(1)

a,b   constants
r   distance between tip and sample

The interaction force (F_{int}) is determined by differentiating the potential:

$$F_{int} = -\frac{\partial V_{LJ}}{\partial z} = -\frac{12b}{r^{13}} + \frac{6a}{r^7}$$

(2)

Figure 18 shows the qualitative characteristics of the LJ-potential which is a superposition of the electron-electron repulsion- (red-dashed line) and VdW-potential (green-dashed line). The green chain dotted line indicates the threshold force of the cantilever and the intersection point B with the interaction force (black line) marks the jump to contact point. By

approaching the sample, the tip gets attracted to the sample after exceeding the threshold force of the cantilever (green chain dotted line) due to the attractive VdW-force (green shaded area). Through further approach the tip gets retracted by the sample due to the Pauli Exclusion Principle indicated by the red shaded area.
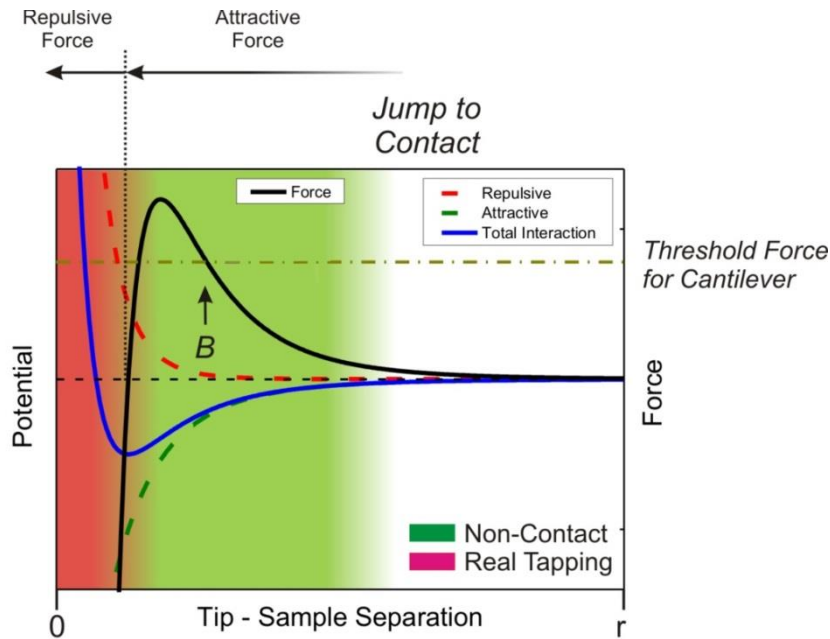
Figure 18: the superposition of the attractive VdW potential (green dotted line) and repulsive electron-electron interaction (red dotted line) results into the total interaction potential (blue line). The intercept point B indicates the jump to contact distance due to the excess of the threshold force of the cantilever (green dot dashed line).[32]

2.3.4 Modes

In contact mode the tip is in constant contact with the specimen surface. The advantages are that high scan rates are possible and an atomic resolution might be possible, however, it could lead to a destruction of the sample, delamination or to a local removal of material as schematically indicated in Figure 19.
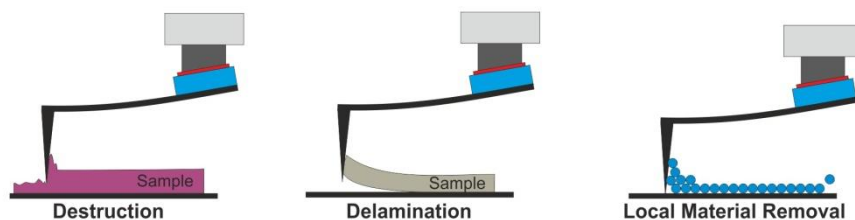
Figure 19: possible problems in contact mode (destruction, delamination, local material removal).[32]

To reduce the interaction of the tip with the specimen the so called tapping mode is used. In this mode the cantilever oscillates with a high frequency (normally in its resonance frequency) and so the tip only taps on the surface. The frequency of the cantilever which is

generated by the piezoelectric crystal is meant to be constant. It has to be considered that the same interactions between tip and sample occur as illustrated in *Figure 18*, leading to a damping of the amplitude. The damping of the amplitude is a combination of energy dissipation, due to the short contact between tip and sample, and a displacement of the resonance frequency through the interaction between tip and sample. Subsequently, the original resonance frequency is reached by moving the cantilever up or down in z-direction leading to information about the height.

Additionally, a phase image is obtained due to the phase shift of the exciting piezoelectric crystal and oscillating cantilever. As the phase shift also depends on the local sample material, information about the material contrast is obtained.
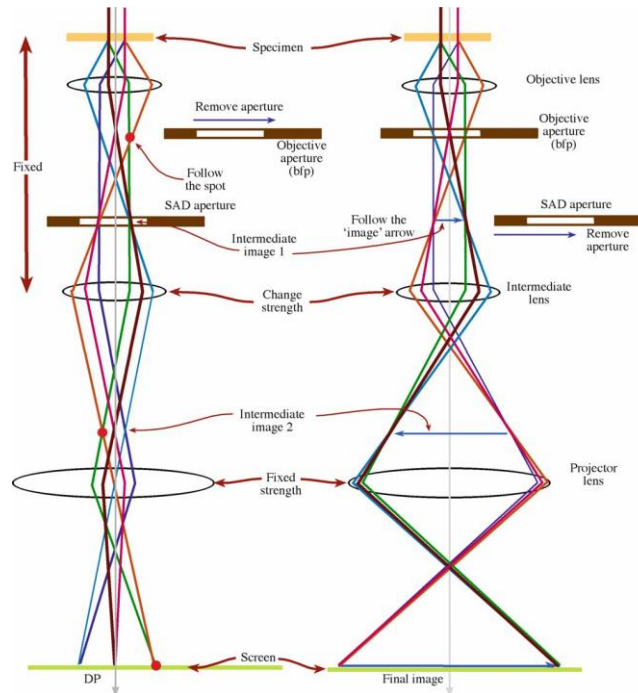
Figure 20: schematic illustration of the two basic modes of TEM imaging systems involving diffraction mode where the diffraction pattern (DP) is projected onto the screen (left) or the image plane of the objective lens (right).[40]

2.4 Transmission Electron Microscope (TEM)

The analysis of structures and of their chemical composition in the nanometer range is the main intension of transmission electron microscopes (**TEM**). Emitted electrons are accelerated up to 300 keV and a condenser lens system is used to illuminate the specimen in TEM mode. However, in scanning-TEM (**STEM**) mode the beam gets focused through the condenser lens system and is scanned over a defined area. A slightly magnified image is generated by an objective lens which gets further magnified by different lenses and finally can be viewed on the fluorescent screen or digitally recorded. Alternatively, a diffraction pattern can be displayed, which is imaged in the focal plane of the objective lens, as schematically illustrated in Figure 20.

High resolution TEM (**HR-TEM**) is used to resolve structures up to 0.1 nm where it is even possible to see atomic columns. TEM images with atomic resolution are results of a phase

contrast developing from electrons diffracted by the crystal lattice by penetration through the specimen. Mainly elastically scattered electrons are used for imaging, however, inelastic interaction processes between sample and primary electron beam provide the needed information for analytical methods. Nearly all chemical elements can be identified by either measuring the energy loss of the primary electrons (electron energy-loss spectroscopy – **EELS**) or by secondary processes due to the transmission of the ionised atom in its ground state (Energy Dispersive X-ray Spectroscopy - EDXS) as explained in detail in section 2.2.3.
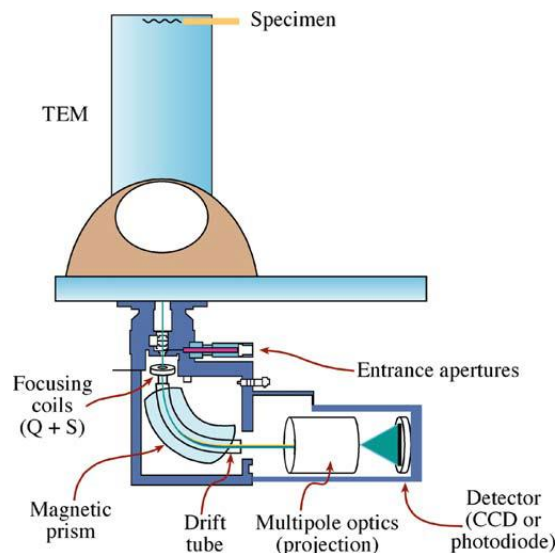
Figure 21: schematic diagram of the EELS showing that it is interfaced below the viewing screen of TEM and indicating the different components.[40]

EELS is used to analyse the chemical composition of small specimen areas up to 1 nm. Electrons with an energy between 60 and 300 keV lose part of their energy due to inelastic scattering by penetrating through a very thin specimen (<100 nm). Inelastically scattered electrons get separated in the magnetic field of the spectrometer due to their energy loss. The spectrum is magnified by magnetic lenses and projected on a CCD-detector, as schematically illustrated in Figure 21. By this method it is possible to analyse elements from He till U. It has to be noted that especially light elements, transition metals and noble earth elements are detected with high efficiency. Elements are clearly identified in an EELS spectrum, due to the facts that electrons ionize atoms by knocking out inner shell electrons. The spectrum shows the element specific ionization edge. The intensity of the ionisation edge enables a chemical analysis of the sample with an accuracy of a few percent. Typical values of the detection sensitivity are in the range of 0.1 to 1 at%, which depend on the composition of the matrix and the specimen thickness. Additionally, information about the chemical bonding states of the excited atoms can be obtained by analysing the fine structure of the ionisation edge. The Energy-Loss Near-Edge Structure (**ELNES**) and the Extended Energy-Loss Fine Structure (**EXELFS**) are used to obtain information on the electronic states, coordination number, oxidation state, band gaps and interatomic distances. The low loss range of the spectrum (<50 eV) emerges because of inelastic interactions with electrons with the valence or conduction band obtaining information about the electrical and physical properties of the specimen.

3   Focused Electron Beam Induced Deposition (FEBID)

3.1   Concept

Focused electron beam induced deposition (**FEBID**) is a maskless direct write method of functional nanostructures in a SEM or DBM. An electron beam locally dissociates precursor material into a volatile and non-volatile part. The non-volatile part condenses on the surface and forms a deposit of predefined shape. It is also possible to fabricate deposits by using ions to induce dissociation which is known as focused ion beam induced deposition (**FIBID**). The principle mechanism is the same, however, the properties of the deposition as volume growth rate, shape and resistivity differ.

The microscope has to be equipped with a gas injection system (**GIS**) containing the precursor material which has to have a low melting- or steam point. Figure 22 illustrates the FEBID/FIBID process: The gas injection nozzle gets placed in a distance of approximately 100 µm above the sample. Next, the gas valve opens and the precursor gas streams out with a comparatively high partial pressure at the area of deposition. The gas molecules physisorp on the substrate, diffuse randomly and desorb again after a residence time depending on a variety of precursor and substrate related parameters. Interaction of the electron/ion beam with the precursor material then leads to dissociation of the precursor material in a volatile and non-volatile part as mentioned above. Volatile products are pumped up by the vacuum system and the non-volatile part grows structures at the position of interaction.

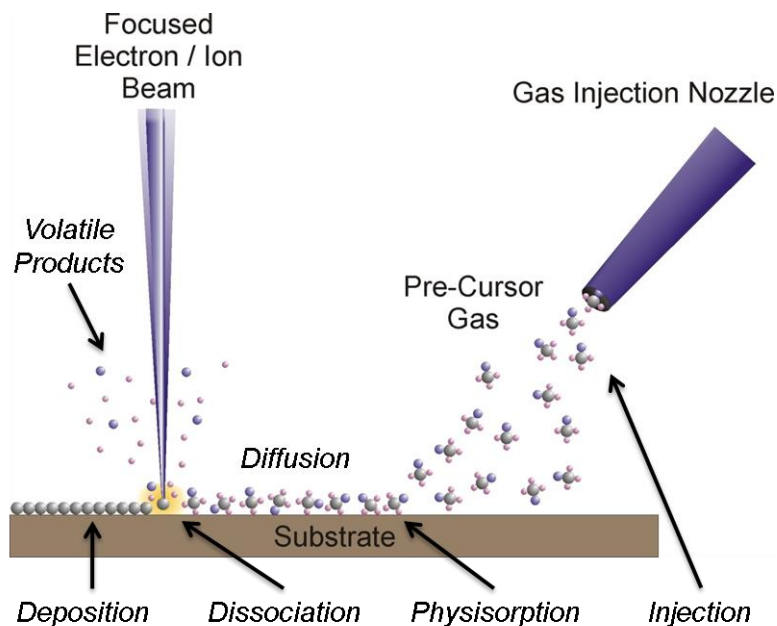*Figure 22: working principle of the FEBID/FIBID process.*[32]

The benefits of FEBID are the absence of special sample preparation before or after the fabrication and the opportunity to deposit on even non flat surfaces down to the nanoscale range.[8] The biggest drawback of this method is the poor metal content of the deposition, as most precursor materials are not available in pure form and broadening of the deposited

structure comparative to the PE beam.[26] Figure 23 shows the elements which have been investigated in FEBID, indicating the best obtained purities in at.% for FEBID deposits. To obtain a pure metal, all ligands which make the metal atom volatile must be stripped. As electron energies reach from electron volts (SEs) to kilo-electron volts (see Figure 4) bond splitting is not selective. Subsequently all different kinds of dissociation products can be formed and contribute to the final deposited structure.[1]

													C 100%				
											Al ★	Si 100%					
	Ti 35%		Cr ★	Mn ⊗	Fe 100%	Co 97%	Ni 36%	Cu 60%		Ga 50%	Ge 100%						
			Mo 10%		Ru ⊗	Rh 66%	Pd >50%				Sn 58%						
			W 66%		Os ⊗	Ir 33%	Pt 83%	Au 100%			Pb ⊗						

Figure 23: periodic table of elements for FEBID indicating the best purities obtained. Percentages are indicated in (at.%), however, the hydrogen content is not considered. ★ indicates that the material is claimed as being pure when deposited, but it is not proven quantitatively, ⊗ means that no quantitative information on the composition of the material is available.[26]

3.1.1 Dissociation Mechanism of Adsorpates

As mentioned above, the electron beam cracks the precursor molecules up, which leads to deposition of nanostructures. It is known that SEs which have energies in the range of 5 – 100 eV are mainly responsible for dissociation of the precursor material, due to appropriate cross sections. This process is known as dissociative electron attachment (**DEA**). However, DEA induces mainly incomplete fragmentation of the parent compound which might lead to an enclosure of non-metal impurities as carbon in the deposition. Dissociation into neutrals or ions have a threshold energy of ~10 eV. Hence, most of the SEs cannot contribute to the dissociation ionization (**DI**) process, because the SEs energy distribution is peaked in the range of 10 eV [28] (see Figure 4). The maximum cross section of dissociation into ions or neutrals is in the energy range of 20-100 eV. PEs can as well contribute to the dissociation process.[1,41]

DEA processes run only in a narrow energy range, however, this energy range is found to overlap significantly with the predicted SEs energy distribution. The DI process takes place in a much larger energy range, but overlaps only with the tail of the SEs energy distribution. Though, DI processes mainly contribute to the deposition of parent compound of the precursor material.[41]

Another reason for SEs-dominated deposition process is that an electron beam with a high primary energy can be focused smaller than a nanometer, so it should be possible to obtain structures with a lateral size comparable to the beam diameter including the SE distribution

range. However, this is not the case as BSE and related SE2 contribute significantly to the deposition process as discussed in detail by Arnold et-al[10].

3.1.2 Working Regime

Depending on the ratio between potentially dissociating electrons and locally available precursor material we distinguish between two extreme conditions:

- In the molecule limited regime (**MLR**) more dissociative electrons are available than required for full dissociation. Due to the excess of electrons it leads to the polymerization of the carbon fragments of the precursor molecules which get incorporated into the deposit.

- The electron limited regime (**ELR**) is indicated by a lack of dissociative electrons in contrast to the available precursor material. Subsequently, precursor material gets incompletely dissociated which will be incorporated into the nanostructures.[8]

In between these extremes there exists a balanced regime leading to lowest carbon contents as extensively discussed by Plank et-al and Winkler et-al.[8,42]

The situation gets even more complicated as the above mentioned conditions assume different but constant surface coverage degrees. In real conditions the final shapes as well as their chemistry strongly depend on the replenishment conditions as well as their directional components as discussed in detail by Winkler et-al [11,42]

Although very important for final FEBID performances, a detailed explanation of precursor surface dynamics would be beyond the scope of this thesis. The most relevant part of this section is the fact that the two extreme conditions lead to different carbon types incorporated into the matrix which will be investigated with respect to the purification results.
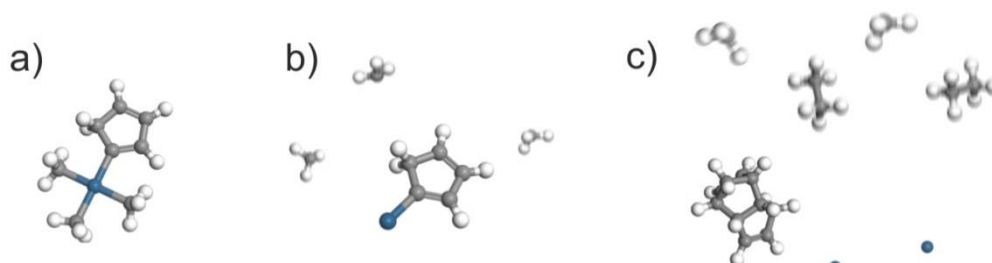

Figure 24: MeCpPt^{IV}Me$_3$ precursor in its native chemical structure (a) where the central blue atom represents the platinum, grey atoms indicate the carbon and the white spheres illustrate the hydrogen atoms; b) partially fragmented precursor material (typical for ELR conditions); c) completely freed platinum compound together with polymerized fragments due to the excess of electrons in MLR conditions. [32]

3.2 Precursor Gas

Figure 23 illustrates possible FEBID precursor materials and indicates their purity. The possible precursor materials are limited, due to the requirements on FEBID materials: It has to physisorp on the surface, the dissociation process should free the parent compound

completely and also boiling point, toxicity/flammability and price of the material have to be considered.[1]

Our deposits were fabricated by using the trimethyl(methylcyclopentadienyl)platinum (MeCpPt^{IV}Me$_3$) precursor, as schematically shown in Figure 24a. The typical case for ELR regime is shown in Figure 24b where the precursor molecule does not get completely dissociated due to the lack of electrons as explained above. An excess of electrons (MLR) releases the parent compound (see Figure 24c), however, induces polymerisation of the precursor material by the excess of electrons.

4 Experiments and Results

In this master thesis a simple and straightforward post growth purification process for MeCpPt^{IV}Me$_3$ based deposits is introduced using an e-beam assisted approach together with room temperature H$_2$O vapour performed in an ESEM. In more detail, 3D, quasi-2D and quasi-1D deposits were fabricated in a DBM, purified via the introduced approach in an ESEM and subsequently characterized by SEM, EDXS, AFM, and TEM. Figure 25 summarizes parameter variation during deposition and purification categorized to deposit dimensionalities. While fully systematic variations are indicated in green, orange fields indicate selective characterization to get a conceptional overview. Red fields indicate further conceivable process parameters which are not investigated in detail during this thesis and act as indicator for further investigations needed to gain a complete insight in process dynamics. Nevertheless, as will be shown during this thesis, the conducted experiments (green and orange) allow full proof-of-concept analysis as essential outcome of this master thesis.
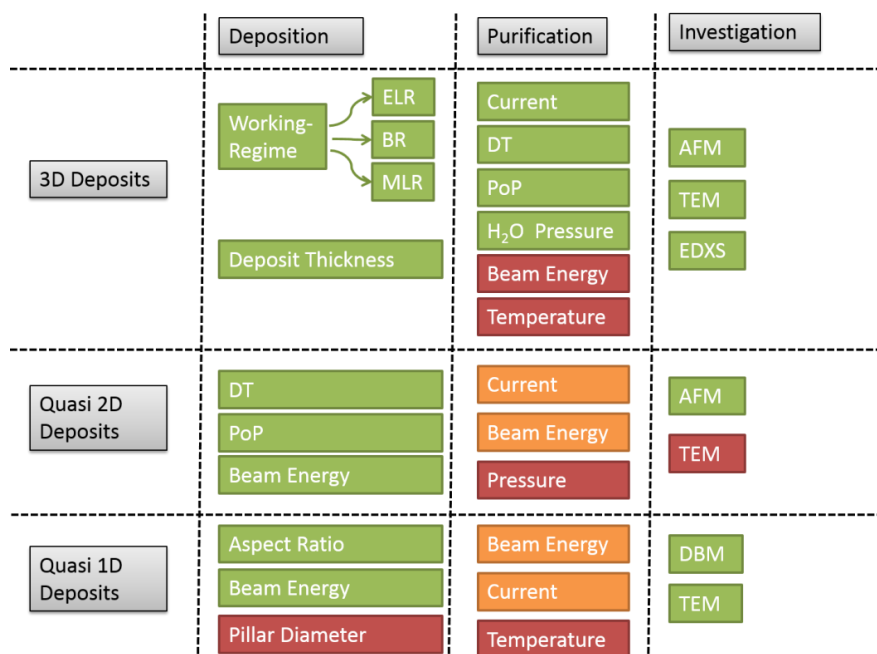

Figure 25: overview of varied deposition parameters (left column) for different dimensionalities (rows) together with parameter variation during purification (central column) and conducted characterization methods (right column). Green and orange fields indicate fully systematic and selective investigations, respectively. Red field complements possible variations which are not investigated in detail during this thesis.

4.1   Experimental Details

In the following the experimental procedures for 3D, quasi-2D and quasi-1D deposits are described while chapter 4.2 and 4.3 gives fabrication and purification parameters in detail.
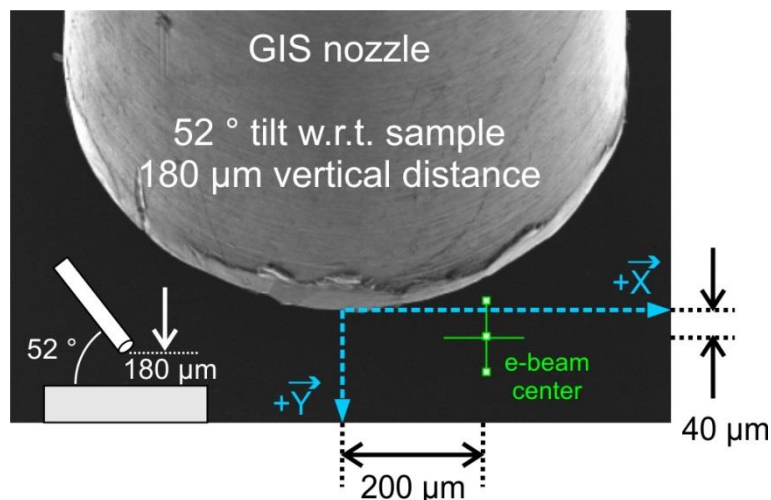

Figure 26: SEM image of the custom-Pt GIS nozzle from the top view. The green cross indicates the position of the e-beam. [27,44]

4.1.1   Experimental Details for the Fabrication/Purification/Investigation of 3-Dimensional Nanostructures

Focused electron beam induced deposition (**FEBID**) was performed with a FIB Nova 200[TM] DBM (FEI, The Netherlands) (see Figure 1). The deposits were fabricated by using the so called *custom-Pt* GIS equipped with MeCpPt[IV]Me$_3$ precursor (see section 3.2). The GIS nozzle was placed in 180 µm vertical distance to the sample surface in tilted arrangement of 52° with a radial distance 204 µm (see Figure 26). Silicon substrates (1 x 1 cm^2) with a 3 nm SiO$_2$ top layer were initially cleaned in a supersonic assisted isopropanol bath for 15 min followed by CO$_2$ spraying and immediate transfer to the DBM. Prior to FEBID the GIS was pre-heated for at least 30 min to 45°C while a background pressure better than 5 x 10^{-6} mbar was established in the DBM vacuum chamber. During this time, the e-beam was focused on a clean sample position using a pre-deposited sharpening array consisting of small Pt-C dots. Then, the e-beam was blanked and the sample was moved in consecutive 50 µm steps so that new nanostructures were always deposited on non-exposed / non-contaminated areas. Next, the valve of the GIS-nozzle was opened for at least 2 min prior to deposition to ensure thermodynamic equilibrium between precursor adsorption and desorption providing constant surface coverage of precursor molecules. 2 x 2 µm^2 deposits were then fabricated via FEBID using the internal patterning engine. The intended deposit thickness was achieved by varying the number of patterning loops together with sample current measurements exhibiting the typical current versus thickness characteristics (see Figure 27) and initial AFM experiments.

Beside deposits with typically flat surface morphologies (see a), it was also investigated whether initial 3D surface features are maintained after purification procedures. For that, bowl shape (Figure 28c) structures were fabricated by using low e-beam currents and DTs of 25 pA and 1 µs, respectively. This leads to diffusion related 3D surface features as relevant

areas are homogeneously covered with precursor molecules at the beginning. Once the deposition process starts, precursor molecules are consumed by impinging electrons leading to local depletion in contrast to unexposed areas in the surrounding of the deposits exhibiting constant molecule coverage. The entailed concentration gradient leads then to molecule diffusion towards depleted areas (= deposition areas). The 3D shape evolves as areas close to the edge and corners are replenished more strongly than central areas of the deposit. The effect is explained in detail in the Master Thesis of DI Robert Winkler[43]. The results can be seen in Figure 39c where edges and especially corners are significantly higher giving the surface a 3D characteristic. The full dependence of surface shapes in dependency on the process parameters is given in Figure 28 and explained in detail by Winkler et-al[42,43].
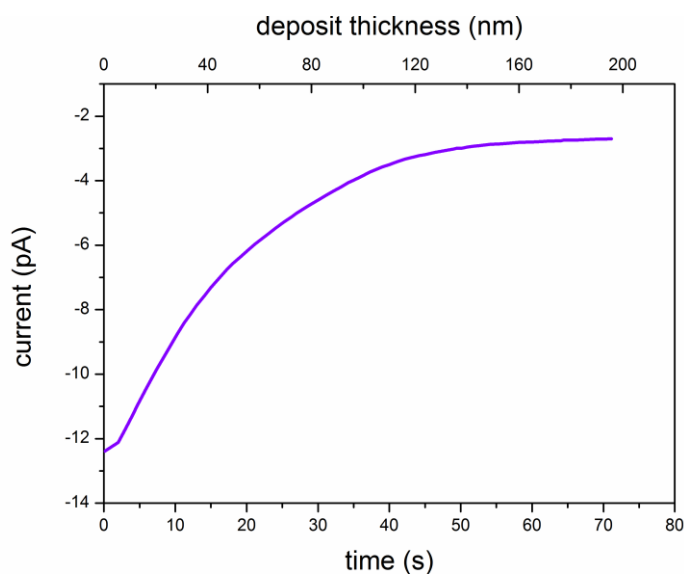

Figure 27: example of sample current measurements for a deposition current of 98 pA at 5 keV, 10 µm DT and 14 nm PoP in order to achieve the intended deposit thickness. A deposit height of 120 nm is estimated at the kink where the current starts to saturate.

After successful fabrication, the samples were immediately transferred to a QUANTA 200 ESEM (FEI, The Netherlands), equipped with an EDXS XL-30 EDXS system (EDAX, USA) which was used for *in-situ* EDXS characterization. Initially, the chamber was evacuated to 3×10^{-6} mbar (**HV**) where the e-beam was focused on the sample surface and relevant purification areas were selected. Next, the intended beam current for purification was chosen via the spot size option and characterized with a Faraday cup (see section 2.2.2). Afterwards, EDXS reference spectra were acquired using 3 min integration time on 4×3.5 µm^2 imaging areas with PoPs and DTs of 4 nm and 1 µs, respectively. In the following the chamber pressure was set to the desired values leading to reduced beam currents of (80 ± 3) % and (50 ± 3) % for 10 Pa and 100 Pa H_2O chamber pressure, respectively, caused by electron scattering in the gas phase. The details of this process are elaborated in section 4.3.5.[37,38] Subsequently, the purification process was started and *in-situ* EDXS spectra were continuously acquired as explained in detail in section 4.3. After purification the ESEM was switched back to HV mode and final EDXS spectra were taken. To get complementary analytical data of fully purified samples, the structures were again transferred to the DBM

microscope which is equipped with a Bruker Xflash 4010 EDXS-system (Bruker AXS) due to higher sensitivity by means of count rates and energy resolution as a result of the installed silicon drift detector (SDD) compared to the Si(Li) detector on the ESEM. All EDXS data were analysed by a semi-quantitative approach as absolute quantification is complicated which is discussed in section 4.4.1.1.
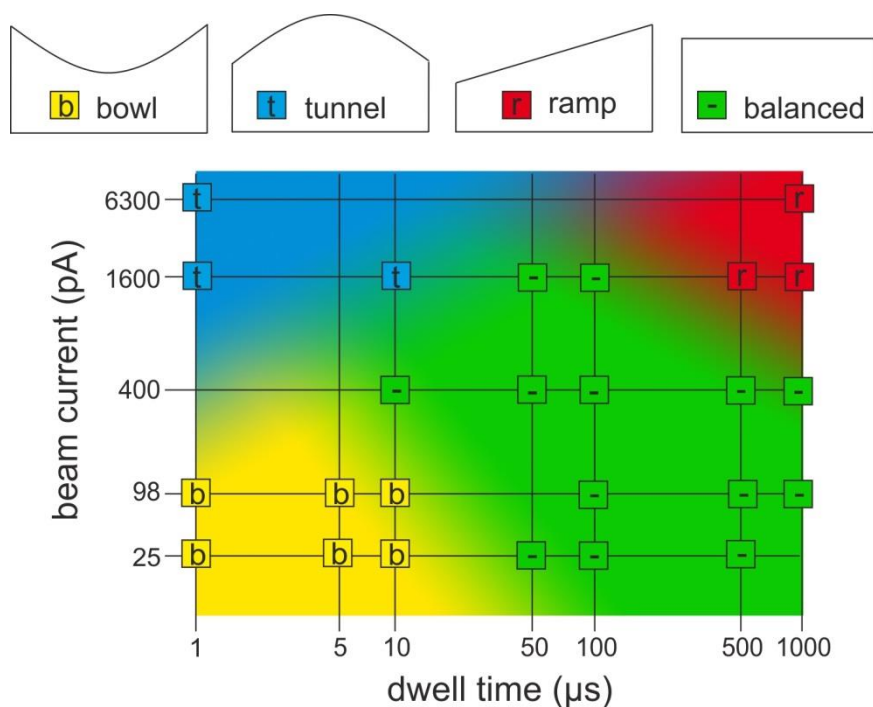

Figure 28: schematic illustration of evolving surface morphologies (top) in dependency on the deposition parameters (bottom) [27,44]

AFM was conducted on as-prepared and purified structures to obtain information of morphology shapes and volume loss. The measurements were performed with a Dimension 3100 microscope (Digital Instruments, Bruker, US) equipped with a Hybrid XYZ scan head and operated with a Nanoscope IVa controller using Olympus OMCL TS-160 cantilever in tapping mode.

TEM lamellas of as-deposited and purified deposits were prepared via focused ion beam processing together with a micromanipulator (OMNIPROBE, US). To identify the boundaries of the Pt layer during TEM, SiO_x top layers have been deposited via FEBID using TEOS precursor. All lamellas were finally thinned down to less than 100 nm for ideal TEM measurements. *All TEM lamellas were gratefully prepared by DI Roland Schmied.*

TEM based measurements were performed on a Tecnai F20 (FEI, The Netherlands) instrument equipped with a Schottky gun operated at 200 kV. In order to record EELS spectra a post column energy filter from Gatan (GATAN, USA) and a 2k CCD was used. EELS measurements were performed in scanning-TEM (**STEM**) mode for a pre-defined area of interest. In order to see the carbon and oxygen K-edges in the same spectrum an energy dispersion of 0.2 eV/channel was chosen. A power law model was used to subtract the background in order to extract the carbon and the oxygen signal. With the background corrected signal elemental distribution maps were created allowing line profile extraction for

carbon and oxygen across the investigated structures. *All TEM measurements were gratefully conducted by Dr. Christian Gspan.*

4.1.2 Experimental Details for the Fabrication/Purification/Investigation of Quasi 2-Dimensional Nanostructures

Quasi 2-D single lines were also fabricated and purified by using same instruments, GIS, precursor, substrate types and overall strategy as described in the previous chapter. In order to receive homogeneously thick lines the quasi-2D structures were fabricated parallel to the long GIS main axis by using the beam scan rotation option (305.5°). The relevance of this relative orientation was previously demonstrated by Winkler et-al[11,42,43]. AFM measurements were performed in same conditions as described in the previous chapter.

4.1.3 Experimental Details for the Fabrication/Purification/Investigation of Quasi 1-Dimensional Nanostructures

Quasi-1D nanopillars were fabricated by the same DBM, GIS, precursor and substrates as described in chapter 4.1.1 In order to allow direct transfer to TEM investigations additional nannpillars have been fabricated on Cu TEM slit grids (OMNIPROBE, US). According characterizations were performed on a Titan[3] (FEI, The Netherlands) equipped with an X-FEG gun operated at 300 kV. STEM-EELS spectra were acquired with a post column energy filter and a 2k CCD (GIF-quantum, GATAN, US) using a dispersion of 0.2 eV/channel. In order to receive the platinum signal a power law model was used to subtract the background. Elemental distribution maps were again created after background correction as explained in chapter 4.1.3. *These TEM investigations on quasi-1D nanopillars were gratefully conducted by DI Angelina Orthacker.*

4.2 Fabrication Details

4.2.1 Fabrication of 3-Dimensional Nanostructures

As known from previous studies[8] the carbon matrices of Pt-C show two different types as already mentioned in section 3.1.2. In more detail, molecule limited regime (MLR) conditions lead to polymerized carbon while electron limited regime (ELR) conditions result in incompletely dissociated precursor molecules incorporated in the carbon matrix. To investigate the influence of the precursor working regime on purification capabilities, Pt-C deposits were fabricated with different purification parameters: *1)* low beam currents of 25 pA (5 keV) with 1 µs DT and 10 nm PoP, to establish ELR conditions; *2)* high beam currents of 1600 pA (5 keV) with 100 µs DT and 26 nm PoP for establishing MLR conditions; and *3)* beam currents of 98 pA (5 keV), 10 µs DT and 15 nm PoP for more balanced regime conditions leading to lowest carbon incorporation due to more ideal ratios between locally available precursor molecules and potentially dissociating electrons.

In order to investigate the dependence on the deposit thickness, 2 x 2 µm^2 Pt-C structures were deposited with a height variation from 30-165 nm and additional step like deposits with a height variation from 30 nm to 300 nm (see Figure 48a) in balanced regime conditions as mentioned in *3)*.

4.2.2 Fabrication of Quasi 2-Dimensional Nanostructures

Quasi-2D single lines were fabricated with an individual length of 1 µm using stream files. In order to investigate most narrow and thinnest lines larger arrays have been fabricated by a systematic variation of PoPs (5, 10, 15, 20 nm) and DTs (1, 2, 4, 8, 16 ms) as shown in Figure 29. All experiments have been performed at 30 keV and 630 pA, due to the absence of a substrate related proximity halo as described in detail by Arnold et al.[10].
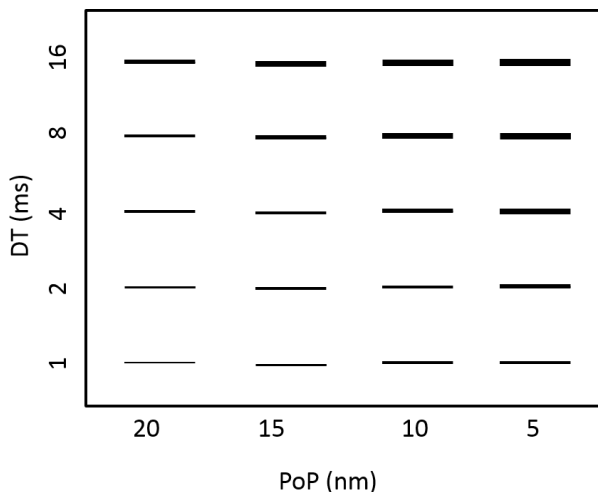

Figure 29: schematic illustration of the array of fabricated lines by systematic variation of PoPs and DTs.

4.2.3 Fabrication of Quasi 1-Dimensional Nanostructures

Quasi-1D Pt-C nanopillars were deposited with a primary energy of 30 keV and 5 keV at beam currents of 21 pA and 25 pA, respectively. All pillars were fabricated in spot mode (constant exposure) and have been separated by about 1 µm from each other. Also different pillar heights were fabricated by different total exposure times based on SEM assisted pre-experiments.

4.3 Purification Details

4.3.1 Purification of 3-Dimensional Nanostructures

All purification experiments were performed in the ESEM (see section 2.2) to provide spatially homogeneous and controllable pressure conditions. Due to the scattering of electrons in H_2O vapour, current measurements were performed in high- and low-vacuum conditions 5×10^{-6} mbar and 10 Pa / 100 Pa, respectively, to estimate local beam currents. Current measurements in ESEM mode were gratefully assisted by Harald Fitzek.[45] For H_2O pressures of 10 Pa and 100 Pa, (80±3) % and (50±3) % of the related HV current remain in a local radius of 5 µm (see section 4.3.5). A detailed calculation of the deposit related full dose is given in chapter 4.3.4.

After acquiring the EDXS reference spectra in HV conditions, the microscope was switched to the intended H_2O pressure of 10 or 100 Pa. Together with the purification process

continuous EDXS measurement were started using an integration time of 3 min followed by a pause of 1 min. In order to investigate how different beam parameters influence the purification process beam currents, DTs and PoPs were systematically varied (values are discussed in detail later) while the scan area was kept constant at 4 x 3.5 µm^2. It is important to note that real purification times are better than stated in this thesis as the purification process itself also takes place while EDXS spectra were recorded. Furthermore, substrate related reference spectra were also acquired in HV and low pressure conditions with same EDXS and scan area conditions to allow subsequent background correction. Finally, EDXS spectra of as-deposited and purified Pt(-C) deposits were taken in the DBM, however, only on 1 x 1 µm^2 sized central deposit areas to minimize substrate related contributions (see section 4.1.1).

4.3.2   Purification of Quasi 2-Dimensional Nanostructures

Quasi-2D single lines were purified with the same experimental strategy, however, without EDXS measurements due to the small line dimensions not providing sufficient X-ray emission. In contrast to the full parameter variation for 3D deposits, single lines were conceptually purified at HV related beam currents of 1 nA and 5 nA (5 keV), ~4 nm PoP, 1 µs DT and a water vapour pressure of 10 Pa. Total purification times were 90 min and 30 min for nominal purification currents of 1 nA and 5 nA, respectively. Furthermore, all lines within an array (see Figure 29) were simultaneously purified using a purification frame size of 12.0 x 10.4 µm^2.

4.3.3   Purification of Quasi 1-Dimensional Nanostructures

Quasi-1D nanopillars were purified at 5 keV using HV currents of 1 nA-5 nA at H_2O pressures of 100 Pa to compensate for massively reduced diffusive replenishment contributions as a result of the enormous aspect ratios for the nanopillars.

Additionally, this high chamber pressure leads to stronger skirt effects which entails that purifying electrons do not only enter the pillars from top but also from the side by laterally scattered electrons (discussed in detail in chapter 4.3.5). Purification was conducted in a scan frame of 14 x 12 µm^2 by using 4 nm PoP and 1 µs DT for 40 min total purification time.

4.3.4   Calculations of H_2O- And Electron-Flux Parameters and Number of Carbon Atoms

The effective H_2O flux for 10 Pa chamber pressure and electron parameters were estimated with the prior introduced method by Plank et al.[7] The effective H_2O flux can be expressed as:

$$\Gamma_{H_2O} = \frac{P}{(2\pi mkT)^{1/2}} \tag{3}$$

P	…	pressure	10 Pa
m	…	molecule mass	18 g/mol
k	…	Boltzmann's constant	1.38x10^{-23} J/K
T	…	temperature	300 K

A value of ~4 x 10^{19} H$_2$O/(cm^2.s) was determined for Γ_{H_2O}. Furthermore, the electron flux is given by:

$$\Gamma_e = \frac{I}{Ae} \tag{4}$$

I	…	current of the electron beam	1-5 nA
A	…	approximate beam size	~30 nm
e	…	charge per electron	1.6x10^{-19} C/e$^-$

It has to be noted that the measured current in HV was used in order to compare it later (see section 4.5) to the obtained values for the oxygen purification.[7] For the effective electron flux Γ_e a value of ~8 x 10^{19} to ~4 x 10^{20} e$^-$/(cm^2.s) was determined. In order to compare the purification processes which were conducted by different parameters as current, scan frame, purification time, the dose (=electric charge/area) was determined by:

$$\text{dose} = \frac{It_p}{A} \tag{5}$$

I	…	current of the electron beam
A	…	area of the scan frame
t_p	…	purification time

Additionally, the number of carbon atoms in a 70 nm thick PtC$_4$ layer with a footprint of 1 x 1 cm^2 was estimated by following relation:

$$N_c = \frac{V \rho N_A n_c}{m} \tag{6}$$

V	…	volume of the nanostructure	1 x 1 x 70 x 10^7 cm^3
ρ	…	density	5.2 g/mol
N_A	…	Avagardo's number	6.022x10^{23} mol
n_c	…	Number of carbon atoms per molecule	4
m	…	molecular weight of PtC$_4$	243 g/mol

This results in an approximated number of carbon atoms N_c of ~$4 x 10^{17}$ for a 70 nm deep PtC$_4$ deposition with a footprint of 1 cm^2.

4.3.5   Skirt Effect for 10 and 100 Pa in ESEM Mode

As already mentioned above for H$_2$O vapour pressures of 10 Pa and 100 Pa, only (80±3) % and (50±3) % of the HV related beam current remain, respectively. However, it has to be considered that the beam current was measured by using a 10 μm aperture as illustrated in Figure 9. This results in the measurement of the not scattered beam including scattered electrons in a radius of 5 μm. Furthermore, it has to be kept in mind that the used scan frame for the purification process was 4 x 3.5 μm^2. Hence, a small fraction of skirt electrons also enter the Pt-C nanostructures. For the investigations in the ESEM a so called X-ray cone

was used to decrease the environmental distance (**ED**), which is the distance between the last aperture to the sample. By using the X-ray cone an ED of ~2.5 mm remains. Though, the electron beam passes also through a complicated pressure gradient between the apertures, which is taken into account by the additional stagnation gas thickness (**aSGT**) (see Figure 6). Including the aSGT leads to a more accurate result rather than just considering the distance that the beam travels through the gas in the chamber (ED).[46]

The aSGT was estimated to be (3±4) mm by considering the diameter of the X-ray cone and the working distance to the bottom of the cone (8.5 mm). Hence, for the SGT (ED+aSGT)[47], a value of (5.5±4.0) mm was determined.[37] Thus, the average number of scattering events per electron *m* is estimated for chamber pressures of 10 Pa and 100 Pa by the following relation[34]:

$$\mathrm{m} = \frac{\sigma(U)}{kT} p\theta \qquad (7)$$

$\sigma(U)$	...	total scattering cross section	0.4×10^{-20} m²/0.7×10^{-20} m²
k	...	Boltzmann constant	1.38×10^{-23} J/K
T	...	temperature of the gas	300 K
p	...	pressure	10/100 Pa
θ	...	stagnation gas thickness	(5.5±4.0) mm

Rattenberger et al.[45] experimentally determined the value for the total scattering cross section σ of H_2O as indicated above (0.4×10^{-20} m²). Danilatos[34] calculated a total scattering cross section σ for H_2O for electron energies of 5 keV of 0.7×10^{-20} m². For the average number of scattering events per electron *m* values of 0.05/0.09 (±0.09) and 0.5/0.9 (±0.9) were obtained for 10 and 100 Pa for the theoretical/experimental determined cross section. It has to be noted that total scattering cross sections of molecules may not just be the sum of the atomic cross sections which was considered for the calculation of the theoretical scattering cross section.[45] Danilatos stated that atomic bindings are responsible for additional interactions that increase small angle scattering.[34]

Out of *m*, a relation of the unscattered beam I and the total beam current I_0 is given by [34]:

$$I = I_0 e^{-m} \qquad (8)$$

Thus, percentages of the unscattered beam gauge to be 95/90 (±8) % and 60/40 (±40) % for 10 Pa and 100 Pa (the first indicated value corresponds to the theoretical calculated value for the total scattering cross section σ and the second to the experimental determined σ). Danilatos[34] showed that for a SGT of (5.5±4.0) mm a half width radius $r_{1/2}$ which contains half of the skirt electrons of 18 (5 35) µm and 22 (5 45) µm develops for 10 and 100 Pa, however, it has to be kept in mind that these values were determined for an electron energy of 10 keV.

The discrepancy between the measured current value at a water vapour pressure of 10 Pa and the calculated value of the unscattered beam can be practically explained by considering the uncertainty, as the measured value is (80±3) % and the calculated value is (93±11) %. It has to be noted that ~3 % of the experimentally determined value are scattered electrons due to the aperture radius of 5 µm as already mentioned above.

As the profile of the scattered electrons remains principally Gaussian[34] and due to the fact that 50% of all scattered electrons are in a range of 22 μm at a H_2O pressure of 100 Pa it can be assumed that 12 % of the scattered electrons are measured with the Faraday cup with the aperture radius of 5 μm for the given technical setup. 12 % of skirt electrons correlate to 7.2 % of the total beam current for a H_2O pressure of 100 Pa, by the assumption that 60 % of the electrons are scattered. This leads to a measured current of ~47 % of the current in HV which is finally consistent with the measured value of (50±3) %.

Figure 30a shows a Matlab simulation of the scattered electron beam travelling through a H_2O vapor of 100 Pa and Figure 30b represents the area of interest (8 x 7 μm^2) by the used scan frame of 4 x 3.5 μm^2 of the Gaussian distribution. In order to visualize how electron skirting influences each pixel of the Pt-C nanostructure by scanning over the used scan frame of 4 x 3.5 μm^2, the Gaussian distribution was "scanned" over every pixel, where 100 x 88 pixels were chosen. Figure 30c reveals the influence of the skirt electrons by scanning over a frame of 4 x 3.5 μm^2 where in Figure 30d the area of influence over the 2 x 2 μm^2 Pt-nanostructure which was placed in the middle of the scan frame is shown. As essence it can be seen that for the Pt-C deposit area (Figure 30d) the scattered e-beam contributes nearly equal to every spot. The different axis scales have to be noted when comparing the individual results.
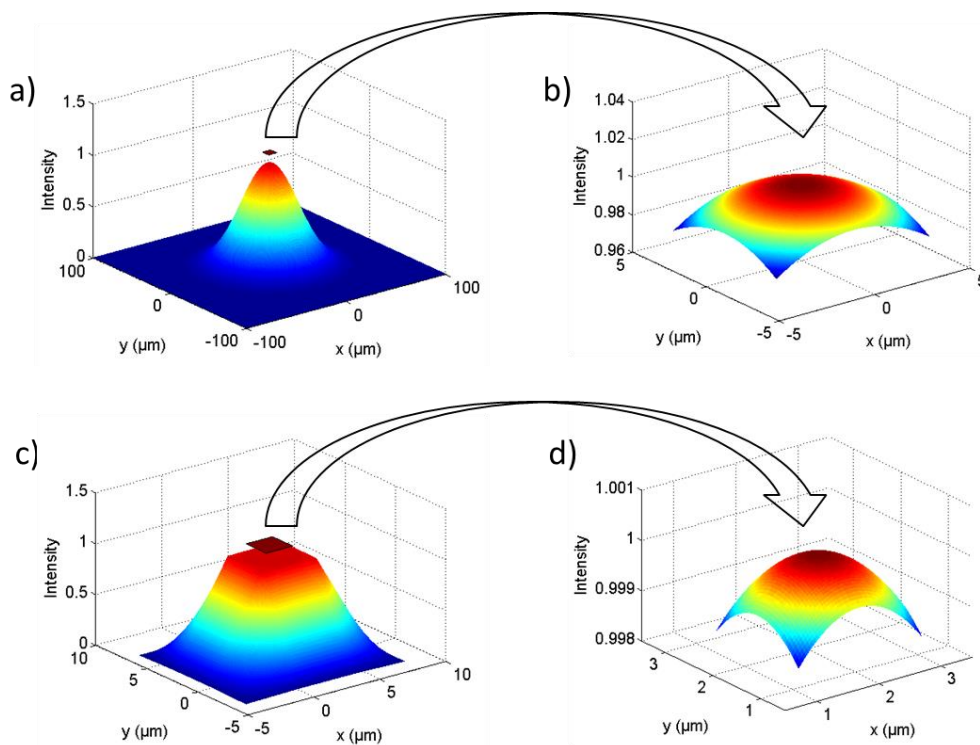

Figure 30: Matlab simulations of the scattered beam at a H_2O pressure of 100 Pa: a) entire Gaussian shaped beam profile; b) area of relevance for purification (4 x 3.5 μm^2) based on (a); c) scattered e-beam contribution for a scan over an area of 4 x 3.5 μm^2 simulated for 100 x 88 pixel; d) deposit related 2 x 2 μm^2 area representing the actual Pt deposit.

4.4 Results

In the following the results are discussed individually for different dimensionalities together with interpretations of the findings.

4.4.1 Results of the Purification of the 3-dimensional Nanostructures

4.4.1.1 Efficiency

As discussed in section 2.2.3, absolute quantification of light elements (e.g. carbon) and thin layers via EDXS is very difficult and prone to strong uncertainties. As an alternative, a previously used semi-quantitative approach was used by deriving relative C/Pt ratio.[7,12,21] First, respective SiO_2/Si reference spectra were used for background subtraction of in-situ / ex-situ spectra following the procedure described in chapter 4.1.1. Subsequently, the C/Pt ratio was calculated by separate intensity integrating from 120-330 eV (C-K and Pt-N, simplified denoted as C-peak) and 1950-2220 eV (Pt-M, indicated as Pt-peak). As reference, a 200 nm Pt layer was characterized via EDXS revealing a C/Pt reference ratio of (0.08±0.01) as the result of Pt-N / Pt-M contributions shown in the upper graph of Figure 31. Additionally, the Si substrate has also a small Si-L contribution in the same area as can be seen by the blue graph in the lower spectra of Figure 31. As direct comparison, as-deposited and fully purified EDXS spectra are given in red and green, revealing the superposition of both Pt-N and Si-L, respectively.
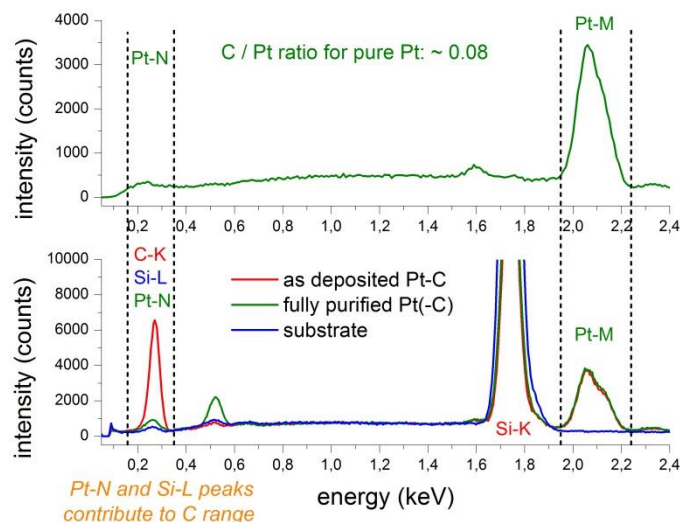

Figure 31: EDXS spectra for pure Pt (top) revealing the Pt-N contributions in the carbon relevant area as can be seen by a direct comparison to as-deposited Pt-C spectra (red graph, bottom). Furthermore, the Si substrate is also contributing in the relevant area via the Si-L peak (blue graph, bottom) which both (Pt, Si) are superimposed to fully purified Pt deposits on Si (green graph, bottom).

It has to be noted that the C/Pt reference ratio varies slightly for different EDXS systems which explains the different ratio compared to previous studies.[7,21] Whereas *in-situ* EDXS measurements were only used to obtain qualitative saturation points, *ex-situ* spectra provide estimations of final carbon contents with respect to the Pt reference spectra. Furthermore, *ex-situ* spectra provide more reliable results as they have been acquired on small, central deposit areas thus strongly minimizing X-ray contributions from surrounding areas. Figure 32 shows a first, representative summary of uncorrected *ex-situ* EDXS spectra after purification at different e-beam currents (see legend) together with the substrate and as-deposited spectra.[12]
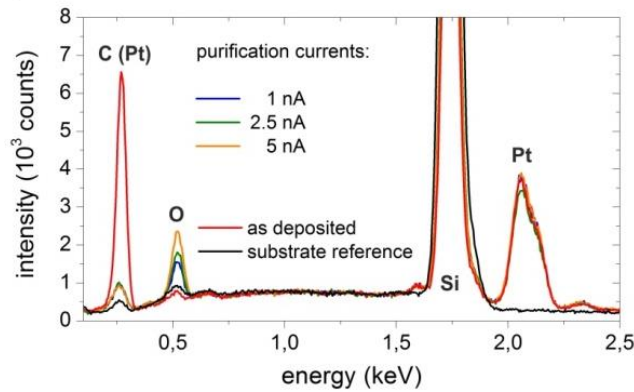
Figure 32: representative summary of uncorrected ex-situ EDXS spectra after 60 min purification at different currents (see legend) together with as-deposited (red) and substrate (black) references. [12]

Initially, the influence of the H_2O chamber pressure was investigated by using a purification beam of 2.5 nA, 4 nm PoP and 4 µs DT. Figure 33 gives the *in-situ* time evolution of the C/Pt ratios indicating the gradual carbon removal for low pressures of 10 Pa and 100 Pa indicated by black squares and red circles at room temperature, respectively. This indicates that the pressure virtually does not influence the purification efficiency and a constant value is achieved after a purification time of less than 2 min.µm^{-2} for the given beam current. Subsequently, it can be assumed that this process is limited by the number of electron- rather than by available H_2O gas molecules. This suggests an electron limited regime for 10 Pa chamber pressure which is highly desirable as it would significantly simplify the technical setup.
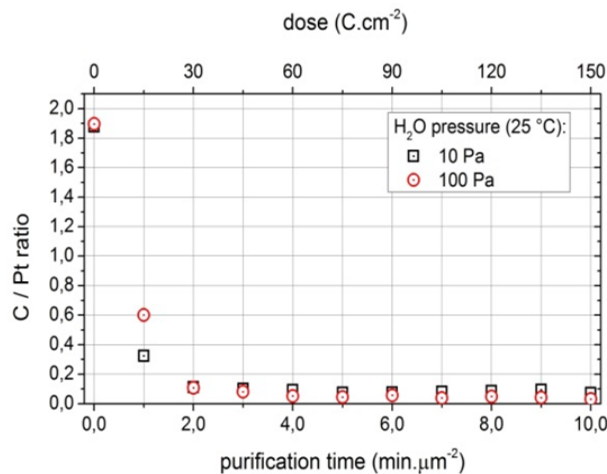

Figure 33: time evolution of C/Pt ratios obtained from in-situ EDXS spectra during purification for H2O chamber pressures of 10 Pa (black squares) and 100 Pa (red circles) including the applied dose on the top axis. [12]

As mentioned in section 3.1.2, the incorporated carbon type depends on the FEBID working regime. Hence, the influence of the working regime was investigated on purification-efficiencies and -rates. PoPs, DTs and H_2O pressures of 4 nm, 1 µs and 10 Pa, respectively, were kept constant for the electron beam assisted purification process while the current was varied from 0.7 nA to 5.1 nA. *Figure 34*b summarizes the *in-situ* C/Pt time evolution of the

purification process for deposits which were fabricated in MLR-regime (top) and ELR-regime (bottom). As expected, the initial carbon content is significantly higher for nanostructure deposited in ELR-regime (initial C/Pt content of ~2.1 compared to ~1.4), due to the incomplete dissociation of the precursor material (see section 3.1.2). It can be noted that the purification rates are not affected by the deposition regime. As expected, higher currents lead to faster purification rates (see Figure 34b). To estimate purification efficiencies the time axis of the obtained C/Pt-ratio from the *in-situ* EDXS spectra of the ELR- and MLR-deposit were re-normalized by the beam current as can be seen in Figure 34a/c (see indications). The normalized curves converge in exception of the two highest currents (dotted and dashed line) resulting from the lack of the *in-situ* time resolution as the process is very fast. All these experiments reveal that 75 nm - 68 nm thick deposits can be purified at rates better than 5 $min.nA^{-1}.\mu m^2$ which are equivalent to a minimum dose of ~30 $C.cm^{-2}$. In more practical numbers, full purification can be done in less than 60 sec for typical beam currents of 5 nA at 5 keV. Again, as no efficiency decay is found for increasing currents, these findings strongly suggest electron limited regime conditions during purification.
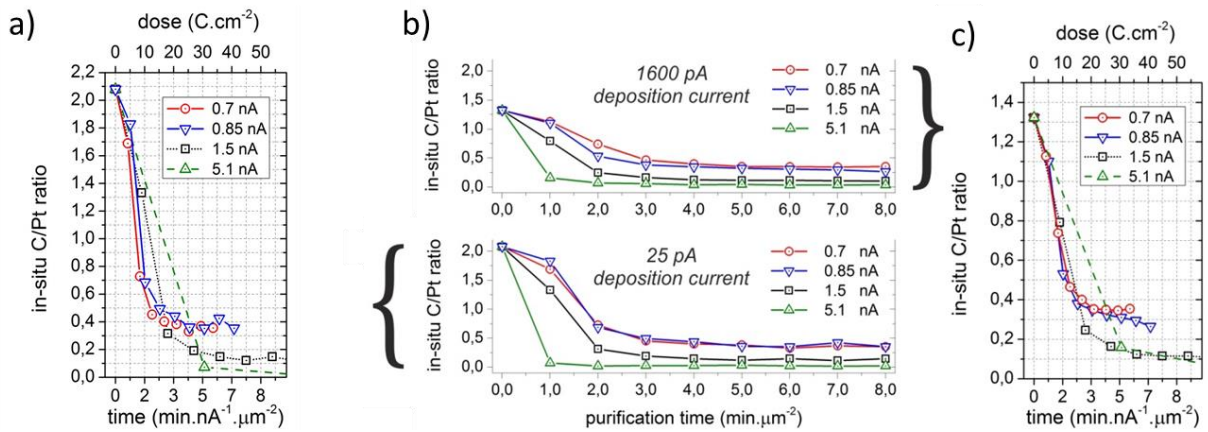

Figure 34: in-situ C / Pt time evolution of purification (b) initially fabricated at very different precursor working regimes leading to different incorporated carbon types (polymerized (top panel) and incompletely dissociated (bottom panel)); a) and c) give the time evolution on current normalized X axes revealing converging behaviour which suggests electron limited conditions during purification. [12]

To investigate the latter indication in more detail DTs during purification were varied by the magnitude of two orders (0.1-10 µs) for different currents as those two parameters typically allow simple control of the working regime. As can be seen for initially 70 nm thick Pt-C deposits there are only weak variations in the decay behavior for both DTs and beam currents. Hence, this is further indication that H_2O pressures of 10 Pa are sufficient to establish ELR conditions over a broad parameter range during purification.

Beside the efficiency, achievable purities were evaluated via *ex-situ* EDXS investigations. Figure 36 shows a total summary of finally achievable purities by means of C/Pt ratios for different beam currents, DTs, PoPs, and H_2O pressures. As can be seen, there is virtually no influence by the purification parameters and the achievable values are very close to the target value of (0.080±0.005) indicated by green shaded areas. This finding does not only support the assumption of electron-limited purification regime conditions but also demonstrates the insensitivity of finally achievable purities with respect to purification

parameters making the introduced process very simple, highly efficient and by that straightforward. [12]
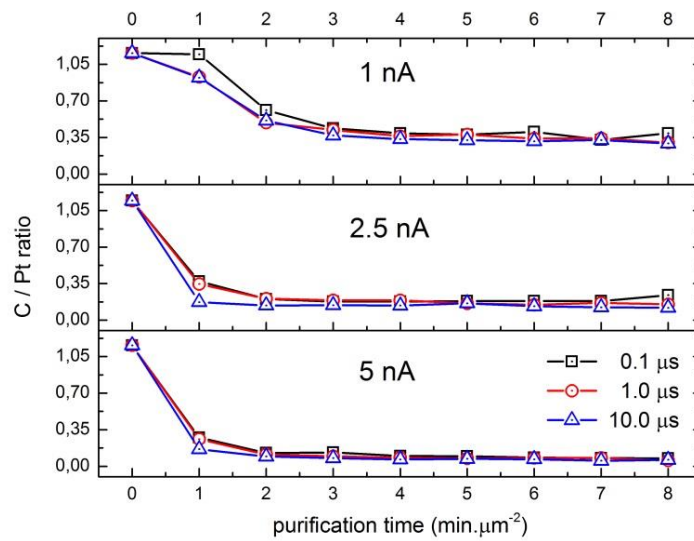

Figure 35: in-situ C / Pt time evolution for initially 70 nm thick Pt-C deposits purified at different currents (different panels) and strongly varying dwell times (see legends). The essence of this summary is the independency on the process parameters which strongly suggest an electron limited working regime during purification at 10 Pa H2O pressures. [12]
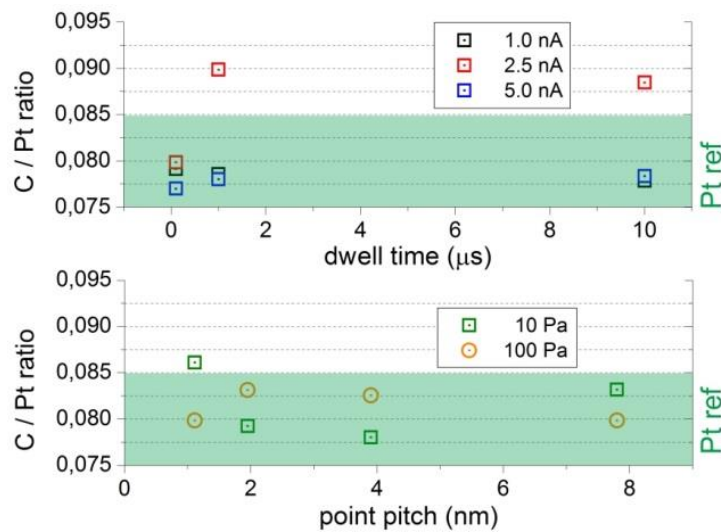

Figure 36: ex-situ EDXS based determination of finally achievable C / Pt ratios for a variety of process parameters during purification. The green shaded areas indicate the target range for pure Pt. [12]
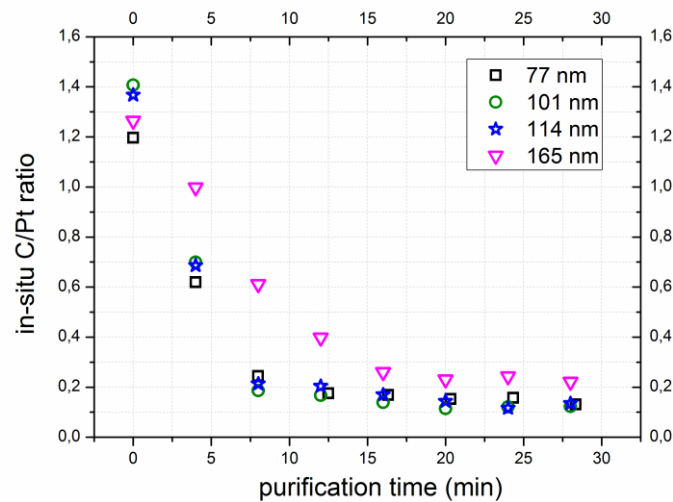
Figure 37: in-situ C/Pt time evolution of purification for Pt-C deposits fabricated in balanced regime conditions for different heights (see legend) (top). The bottom graph estimates minimal purification times for different deposit thicknesses.

Finally, platinum deposits were fabricated in balanced regime conditions with varying deposit heights (77-165 nm) to reveal possible influences on required purification times. Figure 37 shows the according *in-situ* C/Pt time evolution (top) together with an estimation of minimal purification times vs. initial thicknesses (bottom). As can be seen, minimal purification times are equal for deposit heights between 77 nm and 114 nm and increase for thickest deposits of 165 nm. Interestingly, the purification degree (indicated by absolute C/Pt ratios) is virtually the same for all deposits, although previous studies suggested electron depth saturation for depositions of around 80 nm height by using oxygen as purification gas.[21] Recently, Plank et-al. have shown a similar minimal purification time behavior for deposition heights of 5-100 nm which were purified using low temperature oxygen fluxes at 78°C, however, the C/Pt ratio rises significantly for deposits of a height of ~80 nm (see Figure 39).[7] As will be shown later (chapter 4.5) highest efficiencies are found for initial thicknesses up to 150 nm which explains the higher purification time for 165 nm deposits. By that it can be stated that for thicknesses up to 150 nm the efficiency remains the same which makes the process even simpler.
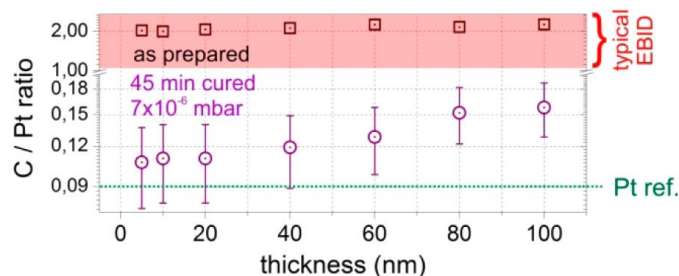

Figure 38: C/Pt ratio for as-prepared and fully purified deposits using low temperature oxygen fluxes at 78 C°. In contrast to our measurements the C/Pt ratios rise significantly for deposits of a height of ~80 nm. [7]

4.4.1.2 Morphology and Shape Fidelity

AFM measurements were conducted prior to and after purification in order to investigate the shape fidelity/quality and the volume loss during purification of Pt-C deposits. *Figure 39*a shows an initially 60 nm thick as-deposited Pt-C structure (left) which was subsequently purified at 5 keV, 1 nA, 1µs DT, 4 nm PoP and 10 Pa H_2O pressure. As can be seen on the right hand side of a) on the same lateral but adapted vertical height scale, the deposit does not show any spatial distortions. More importantly, no pores or cracks have been found even for high-resolution AFM investigations. To investigate the purified structures on lateral shrinking effects, Figure 38b) (upper panel) shows normalized AFM height cross sections as indicated by the dashed lines in a. It can be seen that the pads experience minimal lateral shrinking of less than 4% as Δd ~= 70 nm at full width half maximum which is highly desirable considering the application on much smaller structures.
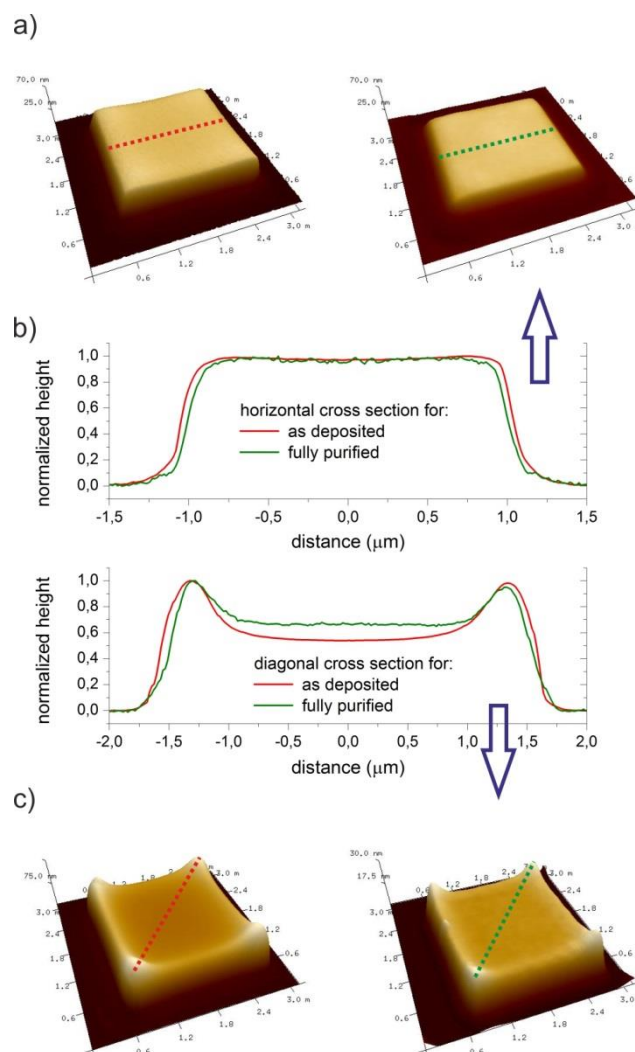

Figure 39: a) AFM height images of as-deposited (left) and fully purified (right) FEBID deposits at same lateral but adapted Z scales to reveal the surface features; c) gives FEBID deposits with 3D surface features before (left) and after (right) full purification again on same lateral but adapted Z scales; b) gives normalized AFM height cross sections accordingly indicated in a) and c) which reveals the maintained lateral dimensions as well as the 3D characteristics. [12]

To investigate whether this purification approach is capable to maintain 3-dimensional surface features bowl shaped Pt-C were fabricated as shown in Figure 38c) prior to purification. The right hand side AFM image gives the fully purified structures with adapted Z-scales. As can be seen, the surface morphology is qualitatively maintained which is compared in more detail by normalized AFM height cross sections in b) (lower panel). Although not perfectly coinciding it is evident that even 3D surface features are maintained after purification which makes this route very promising for more complex 3D structures as will be partly discussed in section 4.4.2.[12]

Detailed roughness analyses were conducted for all nanostructures before and after purification in an area of 500 x 500 nm^2 on central deposit areas. All surfaces showed very similar root mean square values of (0.5±0.1) nm without any cracks or pores. This is one of the major achievements of this thesis as previous attempts in this field, using e-beam assisted O_2 purification at 120°C, revealed excellent purity but massive pores and cracks. [21]

In order to investigate whether the deposit shrinks homogeneously over time or show temporal roughening a time series was performed as indicated in *Figure 40* by AFM height images (top) and absolute cross sections (bottom) according to the dashed lines in the upper row. These images confirm the homogeneous volume loss which is another key feature with respect to partially purified structures for special purposes.
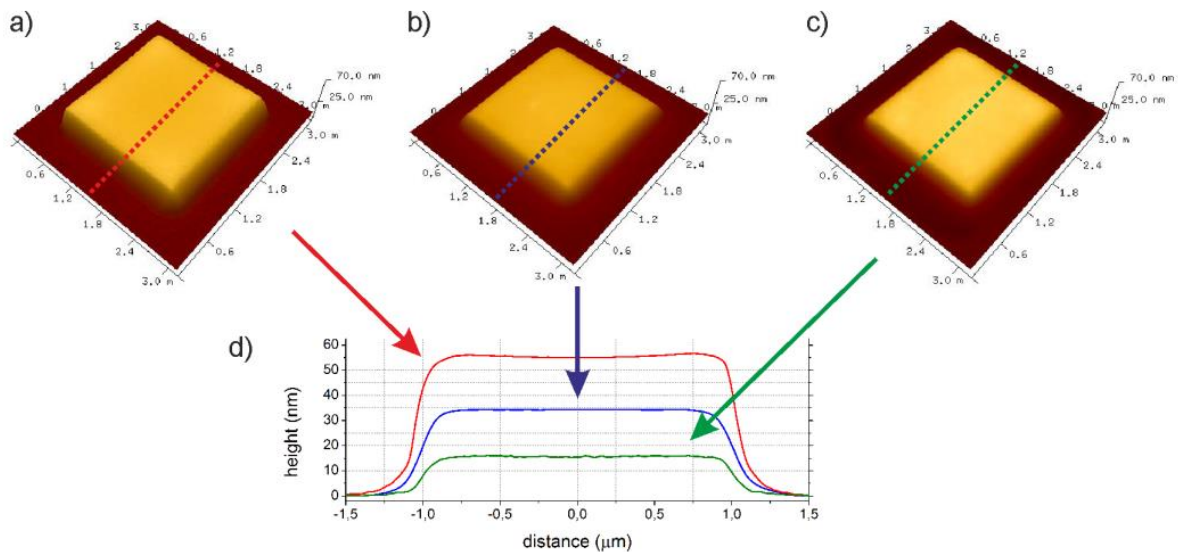

Figure 40: AFM images of Pt-C structures in as-deposited (a), partly purified (5 min 1 nA, 1 µs DT, 5 nm PoP) (b) and fully purified state (c) together with the AFM height cross sections (d) indicated by the dotted line, revealing a mainly vertical shrink. [12]

As already mentioned in section 4.4.1.1, a variation of PoP and H_2O pressures does virtually have no influence on efficiencies or final carbon contents (all deposits are considered to be fully purified as revealed by the *ex-situ* EDXS measurements in Figure 36. However, as can

be seen in Figure 41 different PoPs do have an effect on the surface morphology by elevated edges and corners. As we will discuss later during TEM investigations, these features reveal delamination effects as the purification process is locally incredible due to the longer areal residence time of the e-beam for smaller PoPs. Thus, although ideal by means of efficiency and final purities, very small PoPs can lead to delamination effects. Nevertheless, as has been discussed in the previous chapter, even larger PoPs do not change efficiencies and / or final purities but lead to perfectly maintained deposits shapes. Hence, as a general rule, short e-beam residence times per unit area should be established meaning short DTs and large PoPs which both do not decrease the overall performance.
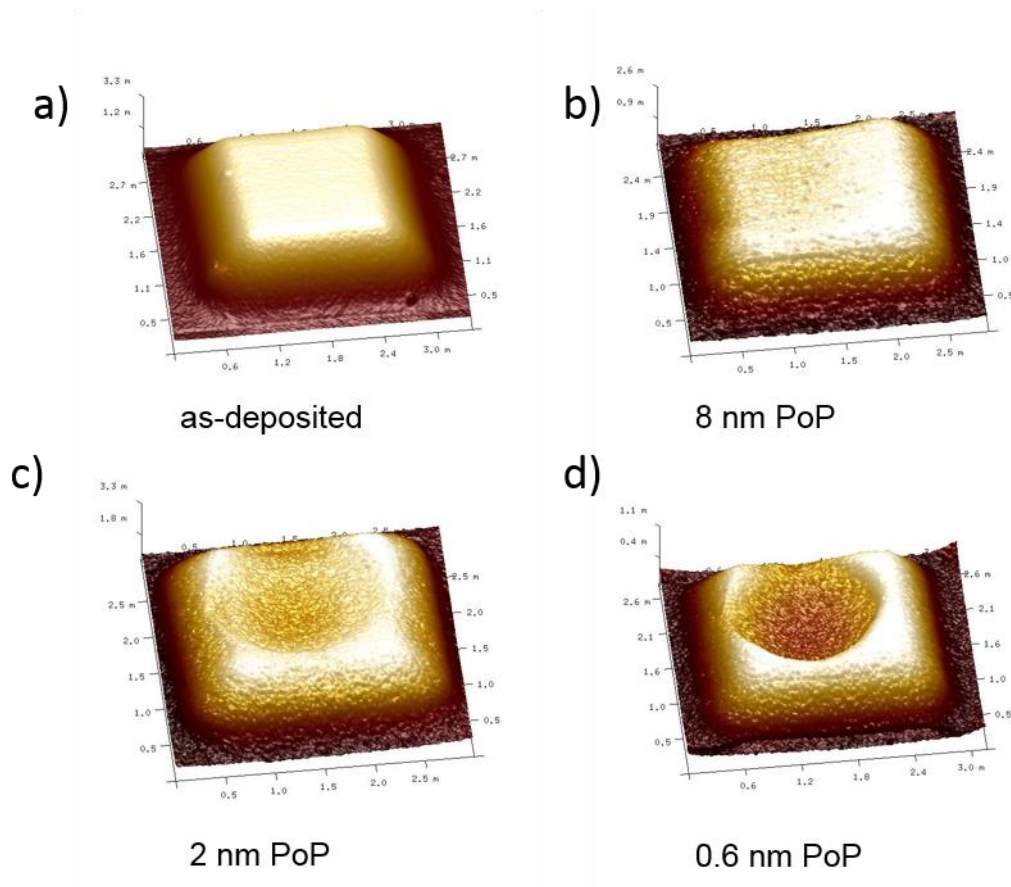

Figure 41: FEBID deposits with an initial thickness of 65 nm after full purification at different PoPs (see indications). Correlated TEM measurements reveal the increased edges and corners as delaminated.

Finally, the volume loss has been evaluated via AFM. For MLR conditions (98 pA, 10 µs DT, 15 nm PoP) a relative volume loss of (69±3) vol.% was found for all deposits which is very close to theoretically predicted values of 70 vol.% based on carbon estimation for according chemistries (estimated by EDXS quantification).[7] On the other hand, deposits fabricated in ELR conditions (25 pA, 1 µs, 10 nm PoP) reveal a higher volume loss of (77±3) vol.%. This is consistent with the observation of higher initial carbon contents as reflected in Figure 34a by the initial C/Pt ratios of 2.08 vs 1.32 for ELR- and MLR-conditions, respectively.

4.4.1.3 Contamination Rim

Beside all advantages of this purification approach, there is one issue representatively shown by AFM images in Figure 42. As can be seen there is an outer contamination rim exhibiting the frame size of the scan frame during purification (4 x 3.5 µm^2). This feature has been observed before by Plank et-al and could clearly be attributed to contaminated samples. Extensive testing revealed that perfectly clean samples (e.g. plasma pre-cleaning or heating) can entirely avoid this feature.
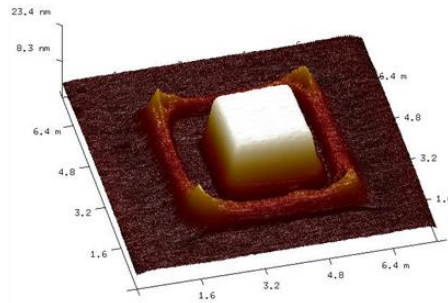

Figure 42: example of a purified Pt structure revealing the unwanted contamination frame only consisting of carbon and oxygen.

Localized EDXS measurements reveal that these frames mainly consist of oxygen and carbon, as shown in Figure 43. AFM images reveal that the contamination rim is higher at corners which can be explained by the diffusion path of the adsorbates: as the electron beam pulses on the same position after every loop the vicinity gets more and more depleted. The surface outside of the frame is fully filled with adsorbates and due to the concentration gradient the physisorbed molecules will diffuse to the scan frame. Before they are able to replenish the central area most of them get already deposited at the edges and corners due to the high current. Subsequently, a rim is deposited with clearly higher corners because of the two different supply directions. Mostly for smaller currents and smaller PoPs the contamination spreads till the deposition. It is assumed that smaller PoPs and currents lead to a slower depletion of the proximity so that adsorbates are also able to replenish areas close to the deposition by diffusion. The intensity and shape of the contamination rim differed from specimen to specimen which is believed to depend on the occurring contamination during the transports. In conclusion, once the rim is initiated it represents a morphological barrier which accelerates the rim growth.

However, as mentioned above, careful pre-cleaning can entirely avoid this feature. Also, there is no Pt found in the rim which would be highly unwanted for real applications. Finally, it should be mentioned that the next step at the FELMI is the implementation of the purification in the DBM making additional contamination during microscope transfer absent.
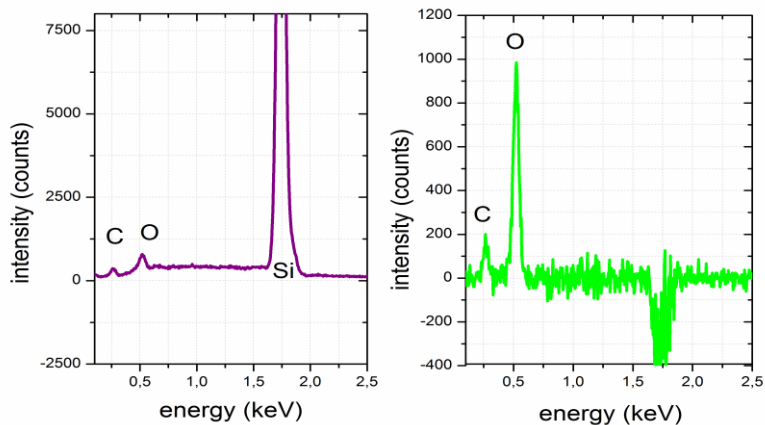
Figure 43: examples of uncorrected (left) and background corrected (right) EDXS spectra acquired from contamination frames as shown in the previous figure.

4.4.1.4 Internal Structure

So far, *ex-situ* EDXS spectra have been used to assess the dynamics as well as finally achievable purities by a comparison to pre-determined Pt reference spectra. However, even in combination with the observed volume loss suggesting complete carbon removal, these techniques do not allow reliable information about the chemistry. Hence, TEM based techniques have been employed to access structural details as well as chemical information using STEM-EELS due to the high sensitivity even for light materials. A variety of different lamellas were prepared in as-deposited, partly, and fully purified states as explained in section 4.1.1.
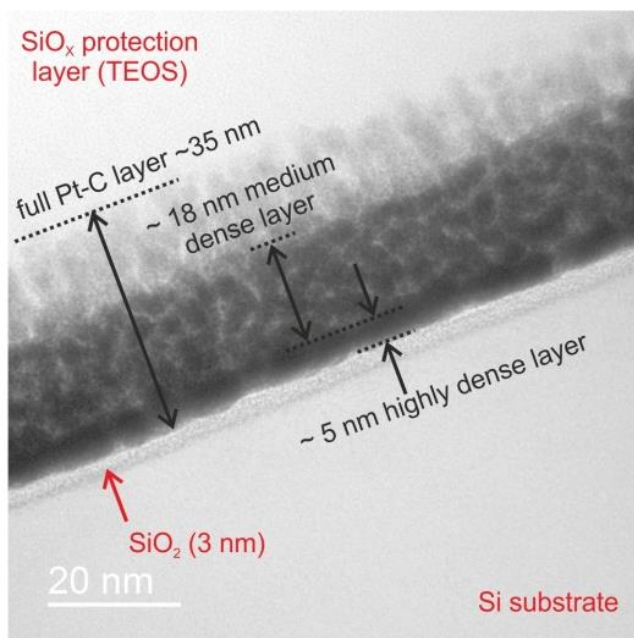

Figure 44: TEM bright field image of a 3 min purified Pt-C deposit (initially 56 nm high) revealing the purification process as a bottom up process. [12]

As starting point the question was addressed whether the purification process starts bottom up, top down, or spatially homogeneous. For that, an initially 56 nm thick Pt-C deposit was partially purified for 3 min (full purification for the used parameters was obtained after about 5 min) and investigated via TEM. As can be seen in Figure 44 by a TEM bright field image, the purification is a bottom-up process as previously suggested by Plank et-al[7]. In more detail, three different zones can be identified as indicated in Figure 44: *1)* a ~5 nm highly dense Pt layer at the bottom; *2)* a ~18 nm medium dense layer followed by *3)* a practically unaffected layer where 2-3 nm thick Pt grains are embedded in the carbon matrix. Below the deposit the Si substrate which is covered by a 3 nm thick SiO_2 layer can be seen and on top of the Pt-C deposit, the SiO_x protection layer (TEOS based FEBID) can be seen (see later in more detail). [12]

As a second step chemical analyses have been performed using STEM-EELS as shown in Figure 45: the top row shows TEM bright field images of as-deposited Pt-C (left) and fully purified Pt layers (right). It is important to note that both images are in scale allowing direct comparison of layer thicknesses and internal structure. The latter reflects the nanogranularity of as-deposited Pt-C layers consisting of 2-3 nm, highly crystalline Pt grains (black dots) homogeneously embedded in a carbon matrix (bright parts in between). After full purification the layer is highly dense revealing crystalline fringes as will be discussed in detail later. The lower graphs in Figure 45 show uncorrected STEM-EELS spot spectra on central areas for as-deposited (red) and fully purified layers (green) in the carbon relevant range starting at ~ 284 eV. The presence and absence of carbon before and after purification, respectively, is clearly evident.
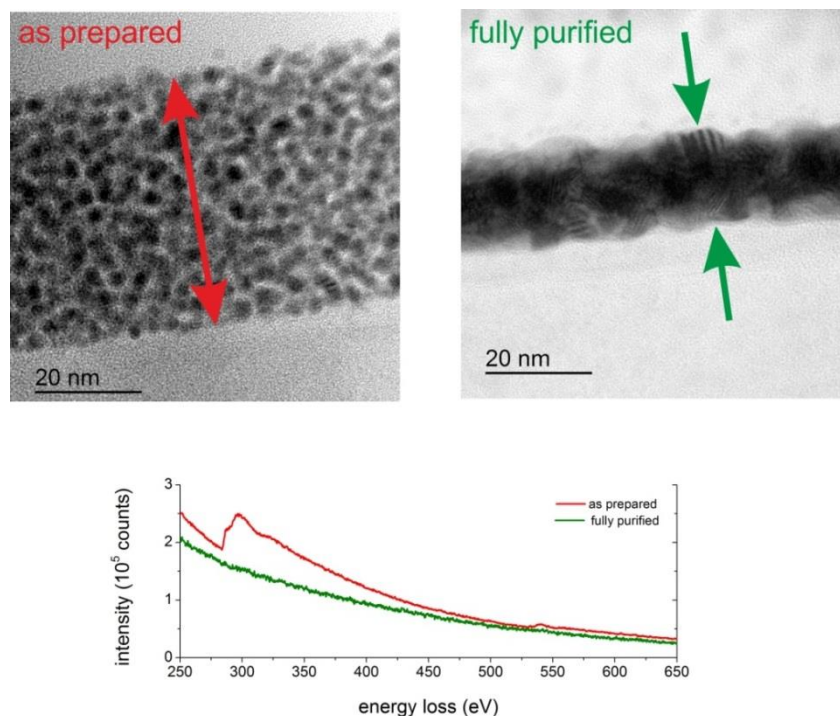

Figure 45: TEM bright field images of an as-prepared (top left) and a fully purified (top right) layer together with the uncorrected STEM-EELS signal (bottom panel) where the red line represents the signal of the not purified structure and the green line for the fully purified layer. [12]
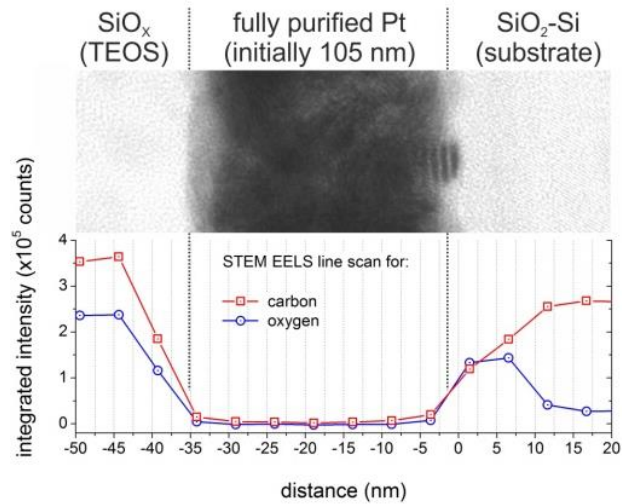
Figure 46: top: TEM bright field image of an initially 105 nm thick Pt-C layer after full purification leading to a highly dense, 35 nm thick Pt layer; bottom: STEM-EELS analysis for carbon (red squares) and oxygen (blue circles) across the fully purified layer shown on top. The oxygen measurements act as interface indicator towards the substrate and the deposit surface which was covered with TEOS based SiO2. The essence of this combined figure, however, is the proof of entire carbon removal after the introduced purification approach. [12]
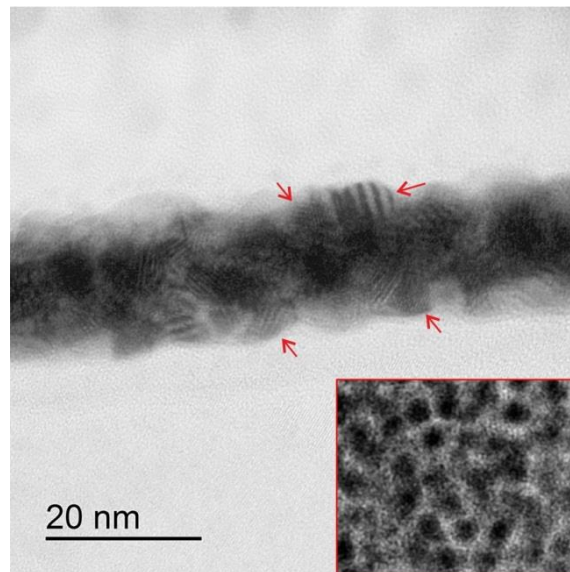

Figure 47: direct in-scale comparison of the grain size via HR-TEM of a fully purified structure (large image) and an as-deposited layer (inset). Furthermore, the red arrows indicate larger Pt crystal grains in the range of 6-9 nm compared to 2-3 nm for as-prepared layers. [12]

Although these measurements clearly indicate the absence of carbon after purification the question remains whether the carbon is removed across the entire layer or e.g. some carbon remaining can be found at the bottom as it cannot diffuse outwards. To clarify these questions, STEM-EELS line scans have been performed across fully purified layers, initially 105 nm thick. Figure 46 shows a TEM bright field image of the investigated layer on top

followed by an in-scale line scan of carbon (indicated by red squares) and oxygen (blue circles) on the bottom. The latter was used to identify the interface to the SiO_2 substrate and the top surface due to the TEOS based SiO_x protection layer. As can be seen, the carbon signal (red-squares) correlates well with the oxygen increases at both interfaces and confirms entire carbon removal across the purified layer (dose > 30 C.cm^{-2}, see Figure 33). These experiments are of essential importance as they support the EDXS based findings of fully purified layer and also point out the validity of in-situ measurements with respect to their saturation behavior.

A closer look via high-resolution TEM (HR-TEM) revealed two details as can be seen in Figure 47: *1)* highly dense packing of Pt grains which are *2)* slightly increased compared to as-deposited grains. The latter can be seen by an in-scale comparison in Figure 47. Closer measurements based on the crystalline features allowed to estimate the grain growth from about 2-3 nm to 6-9 nm after full purification. These findings might also explain the absence of any porosity as not only the carbon is removed but also the grains start to grow during purification.

Finally, a stair like deposit was fabricated with a dimension of 10 x 2 µm^2 in balanced regime conditions using 5 keV, 98 pA 10 µs DT and 15 nm PoP followed by purification at 5 keV, 5 nA, 4 nm PoP, 1 µs DT and a H_2O pressure of 10 Pa with a total dose of ~600 C.cm^{-2}. Figure 48a shows an AFM height image after fabrication with deposit thicknesses of 30 nm, 60 nm, 100 nm, 150 nm and 300 nm. Figure 48b gives the same structure after full purification revealing final thicknesses of 13 nm, 20 nm, 31 nm, 49 nm and 95 nm. The thickest deposit (initially 300 nm), however, revealed again strong delamination effects which was proven by TEM investigations. Figure 48c shows a TEM high angular annular dark field (**HAADF**) image of the initially 300 nm structure where the delamination at the edges is clearly visible. As can already be seen in this image the layer does not show a homogeneous brightness which indicates different purification degrees at different depths.
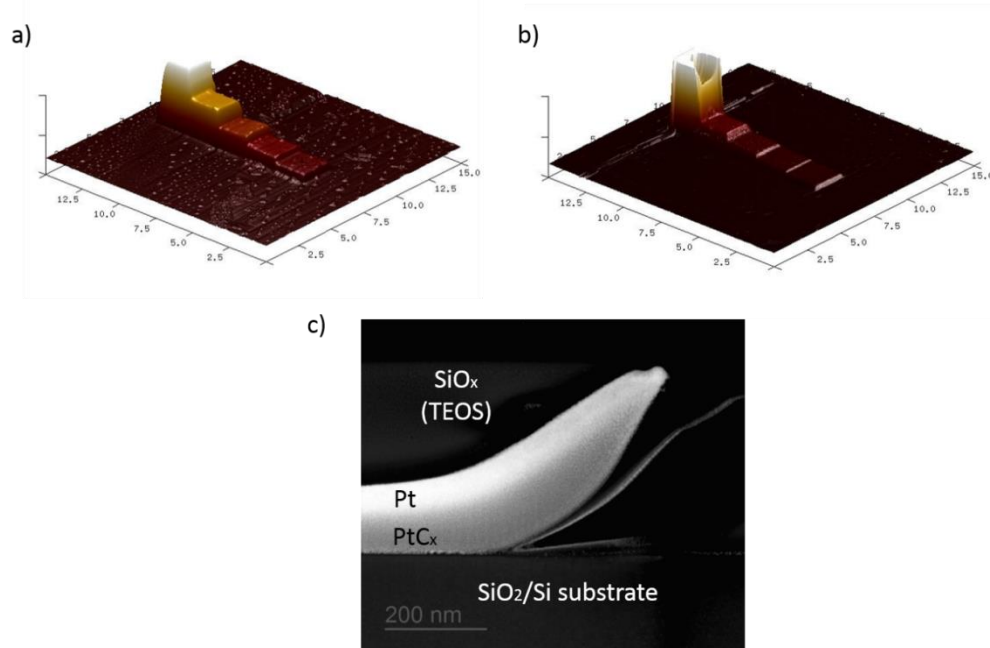

Figure 48: AFM height images of a stair like deposit before (a) and after (b) full purification on same lateral and Z scales for direct comparison; c) shows a TEM HAADF image of the highest deposit (initially 300 nm thick) after purification which reveals the delamination of edges.

To investigate this observation in more detail, STEM-EELS line measurements were conducted across the layer as summarized in Figure 49. The top image is a TEM bright field image of the fully purified layer (initially 300 nm thick) at central areas. The bottom graph gives according STEM-EELS line scans for carbon and oxygen. The latter allows again identification of the interface and the deposit surface by the strong increase (blue circles). In agreement with the HAADF TEM image in Figure 48c it can be seen that only the topmost 45 nm are entirely totally purified and free of carbon. STEM-EELS measurements reveal then a ~ 50 nm thick layer underneath with increasing carbon indicating partial purification. Considering again the delamination together with the inhomogeneously purified layer stack it follows that at the deposit edges there are a kind of bilayer with full and partial carbon removal for top and bottom regions. Taking the according difference in volume loss into account as well it follows that the edges show strain effects which lead to the delamination as the topmost layer contrasts more than deeper layer regions. This explains the observed delamination effects by either too thick layers (Figure 48 and Figure 49) or by inproperly set process parameters (PoPs, DTs) as discussed in chapter 4.4.1.2.
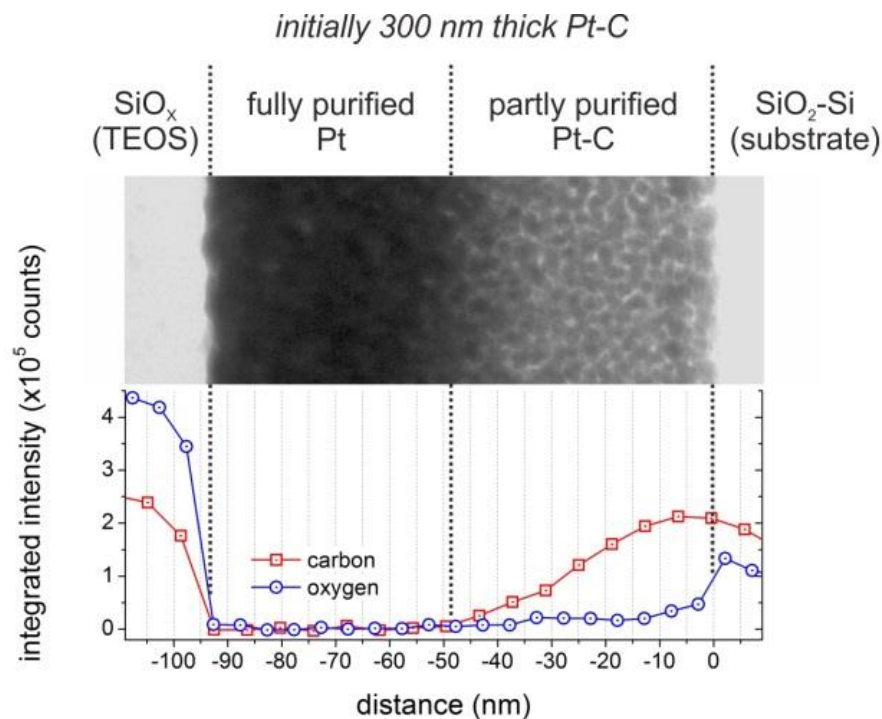

Figure 49: TEM based investigation of an initially 300 nm thick layer after full purification taken at central deposit areas. The top image gives the TEM bright field image while the lower graphs show the correlated in-scale STEM-EELS line scans for carbon (red squares) and oxygen (blue circles).[12]

The observation of incomplete purification for too thick layers raises the question about the maximum initial layer thickness allowing full purification. The next height of the stair like deposit shown in Figure 48 was initially 150 nm thick and shrunk down to 49 nm after full purification. Figure 50a shows the according HR-TEM image which reveals full purification across the entire layer, again accompanied by a slight growth of the Pt grains to about 6-9 nm. Same results are found for initially thinner deposits as summarized in Figure 50b-d.

Hence, it can be stated that initial layer thickness up to 150 nm can be fully purified with the introduced approach. This is also consistent with the efficiency measurements in Figure 37 where the thickest layer of 165 nm showed slightly higher purification times. At this point it has to be mentioned that the discussed observations need to be correlated with Monte Carlo simulations of electron trajectories with respect to their penetration depth in order to explain the limited purification depths. This will be discussed in detail in section 4.5.
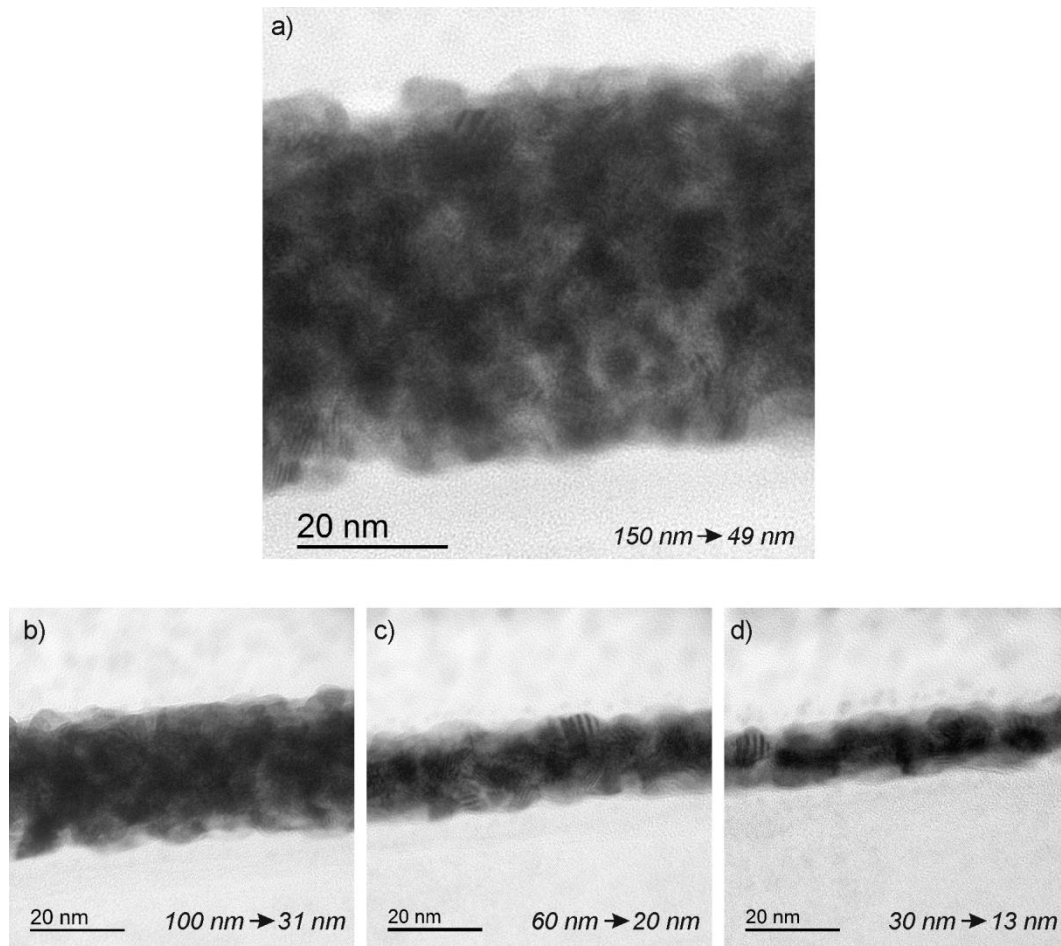

Figure 50: HR-TEM images of fully purified layers taken from central areas. The before and after thicknesses are indicated bottom right.

4.4.2 Results of the Purification Process of Quasi 2 Dimensional Nanostructures

As summarized in Figure 29, single lines with varying PoPs and DTs were fabricated at 30 keV and 630 pA and subsequently purified by beam currents of 1 nA and 5 nA (5 keV) at a H_2O pressure of 10 Pa with a total dose of 20 C/cm^2 and 100 C/cm^2 . AFM images were taken before and after purification to evaluate shape fidelities and volume losses. Figure 51 shows AFM height images (same XYZ scales) of two representative lines before (a) and after (b) purification at 5 nA with a dose of 100 C/cm^2. As it is evident the single lines are disrupted by means of pores and/or cracks but show a height decrease from 15.5 nm to 4.5 nm at very

similar widths. A closer look at the surface, however, reveals slight surface features of fully purified lines as can be seen by the 2D AFM height image in Figure 51. According roughness analyses confirm this impression by an increase from about 0.6 nm to 1.3 nm (RMS) which is not surprising considering the observed grain growth discussed in the previous chapter together with the very thin nature of final lines (4.5 nm).
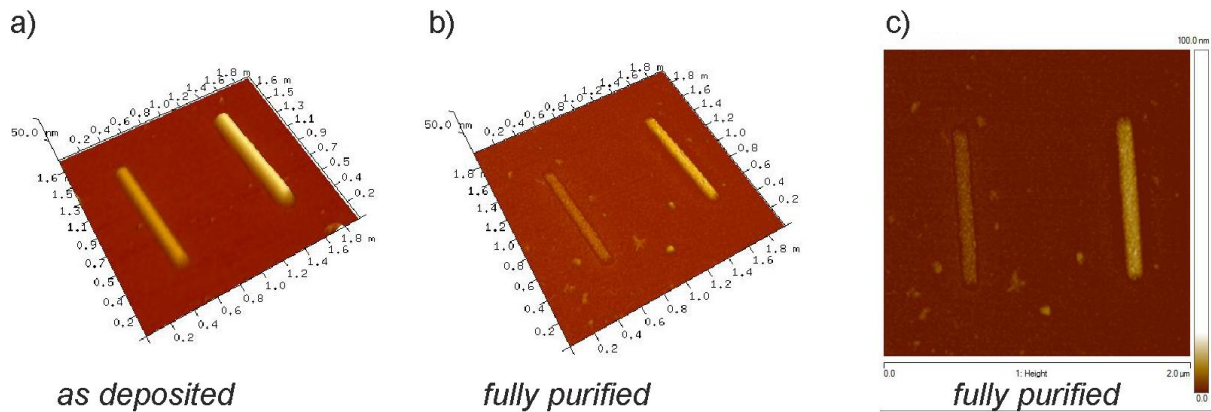

a)   b)   c)

as deposited   *fully purified*   *fully purified*

Figure 51: AFM height images of two representative single lines fabricated at 30 keV, 630 pA, 15 nm PoP, 4 ms DT (left lines) and 8 ms DT(right lines) via single passes. a) and b) show the lines in same scale before and after purification, respectively. A 2D scan is given in c) revealing slightly grainy surface features for fully purified lines also reflected in slightly higher RMS roughness of 1.3 compared to 0.5 nm for as-deposited lines.

Figure 52 compares AFM height cross sections of different single lines (see legend) before (a) and after 30 min purification at 1 nA (b) and 5 nA (c). It is found that the single lines reduce their height by ~13% for 1 nA while a purification current of 5 nA leads to vertical height decrease by ~55 %. The important detail, however, is the observation that the single lines show only minimal lateral shrink which is highly desired considering more complex structures such as rings. To investigate the lower effect for 1 nA in more detail, the purification time was increased to 60 min equivalent to 40 C/cm^2 total dose. The results can be seen in Figure 53 which illustrate that there is virtually no difference between a purification time of 30 and 60 min. This strongly suggests that not only the dose but also the spatial electron density is relevant for final purification performance. Furthermore, it has to be kept in mind that initial line thicknesses are very low which lead to deep penetration of electrons into the substrates reducing the total number of purifying electrons within the single lines. The logical step would be a reduction of the primary energy in order to keep the interaction volume closer to the single lines resulting in a higher spatial electron density of appropriate low energy electrons (preferable SEs). These aspects are discussed in more detail in chapter 4.5 where Monte Carlo simulations are discussed. Finally, it should be mentioned that the single lines revealed initial full-width-half-maximum widths of about 100 nm which is slightly above the possible values around 60 nm for the used currents. We attribute this deviation to a not perfectly focused electron beam which, however, does not contradict the main findings of widely smooth, pore free and fully purified single lines achievable with the introduced purification approach.
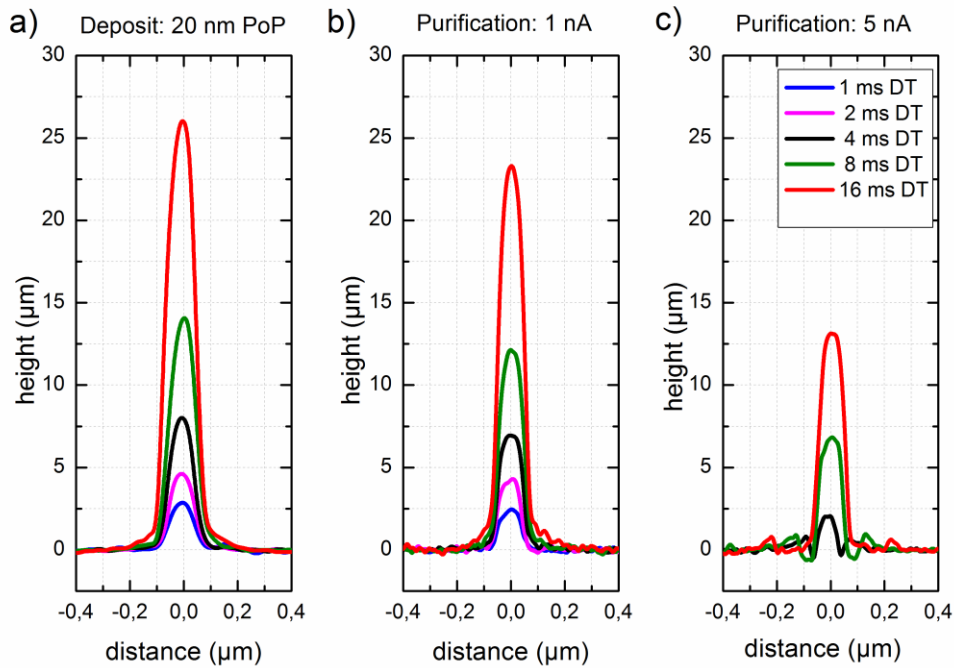
Figure 52: direct comparison of AFM height cross sections of single lines fabricated at 30 keV and 630 pA with 20 nm PoP but different DTs (see legend). While a) gives the as-deposited dimensions, b) and c) show the results after 30 min purification at 1 nA and 5 nA, respectively, demonstrating the height decrease at widely constant base widths.
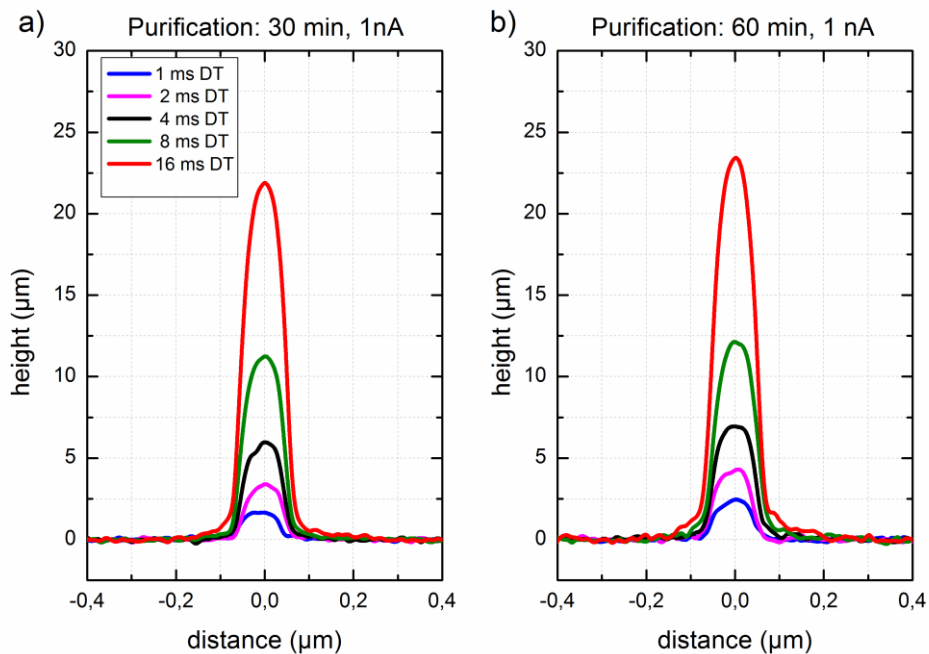

Figure 53: direct comparison of AFM height cross sections of single lines purified at 1 nA for 30 min (a) and 60 min (b) where no further difference can be observed.
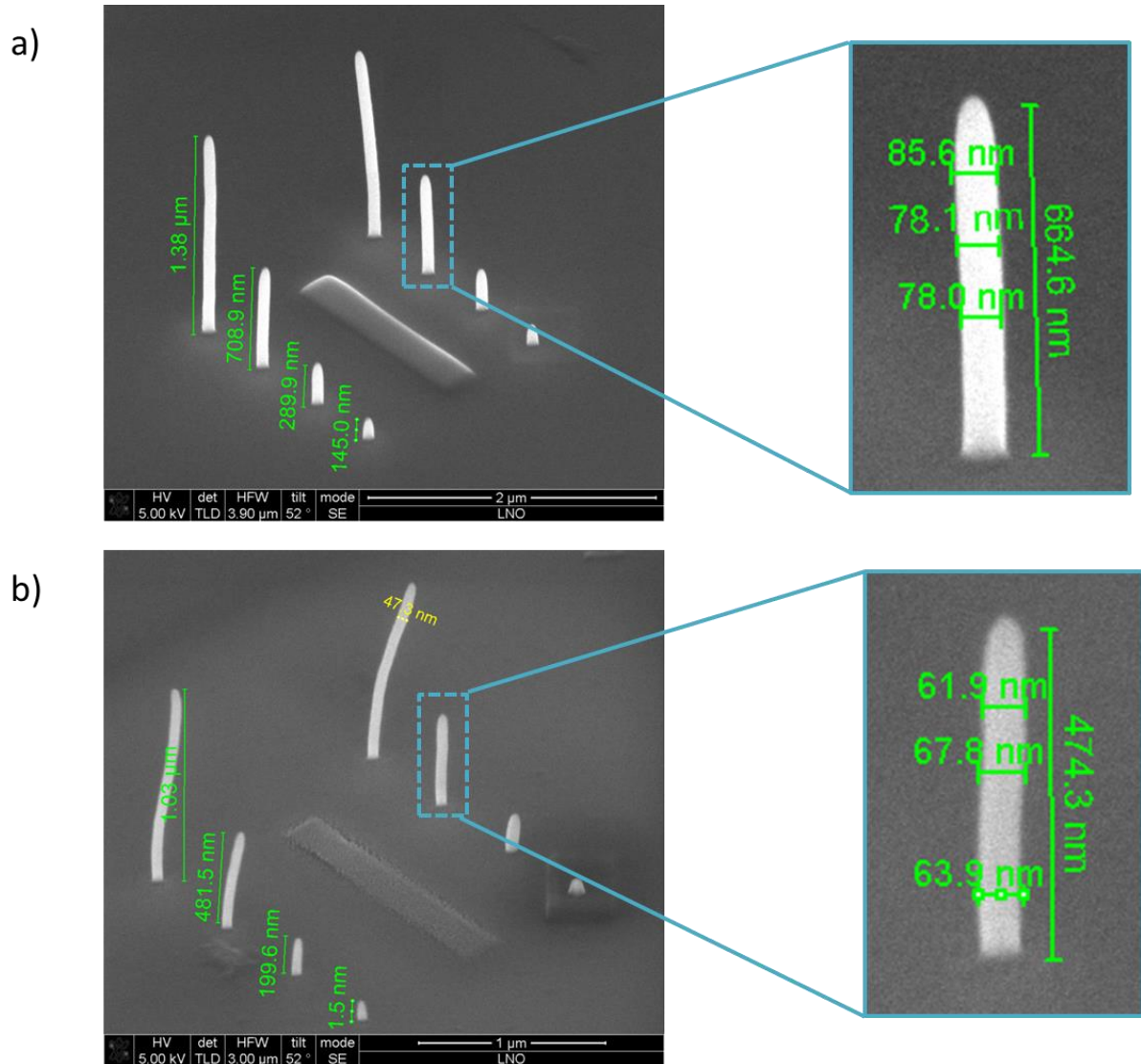
Figure 54: SEM images of an as-deposited (a) and fully purified (b) pillar array using 5 keV and 5 nA during purification at 100 Pa.

4.4.3   Results of the Purification Process of Quasi 1 Dimensional Nanostructures

In order to investigate the possibility of purifying quasi-1D structures nanopillars with different heights ranging from ~160-1400 nm were deposited on a Si/SiO$_2$ wafer with an e-beam current of 25 pA at 5 keV in spot mode (constant exposure). Subsequently, they were purified by using 10 keV and 0.5 nA as well as by 5 kev using 0.5 nA and 5 nA at a chamber pressure of 100 Pa. SEM analysis in tilted arrangements were conducted before and after purification where it is found that beam currents of 0.5 nA (5 keV and 10 keV) do not change the dimensions which is in agreement with the single line results also suggesting very low effects for low purification currents. However, as summarized in Figure 54, a beam current of 5 nA shows a clear difference between before (a) and after (b) purification. Cross sectional measurement reveals a vertical and lateral shrink by about ~30 % and ~20 %, respectively. The combined volume reduction is more than 55 vol. % which suggests almost entire purification of the nanopillars based on dimensional characterization. Although, discussed in the next section in detail, it should be mentioned at this point that the vertical penetration

depth of electrons in the original Pt-C material is less than 250 nm and less than 120 nm for fully purified pillars. Considering now the widely homogeneous thickness of the purified pillars in Figure 54b (right image) together with the total height of more than 470 nm it becomes obvious that the electrons cannot enter deepest areas from top. To explain these observations we have to consider the high chamber pressure of 100 Pa and the entailed skirt effect leading to a certain fraction of electrons which can laterally enter the pillar. This can then explain why also areas deeper than the interaction volume can be purified which should then allow to purify even higher structures.

In order to get spatially resolved structural insights TEM investigations were conducted which used quasi-1D nanopillars deposited with different heights directly on proper TEM grids which exclude further preparation steps. Figure 55 compares low aspect ratio pillars before (top) and after (b) purification via HAADF TEM images. As can be seen the pillar is again shrinking in both dimensions while the material related contrast strongly increases after purification. STEM-EELS line scan measurements were then conducted along purified pillars as indicated in the top image in Figure 56. The lower graph shows the STEM-EELS result for Pt revealing constant intensity. This strongly suggests a homogeneous spatial distribution of Pt along the pillar which supports the interpretation of laterally entering electrons during purification.
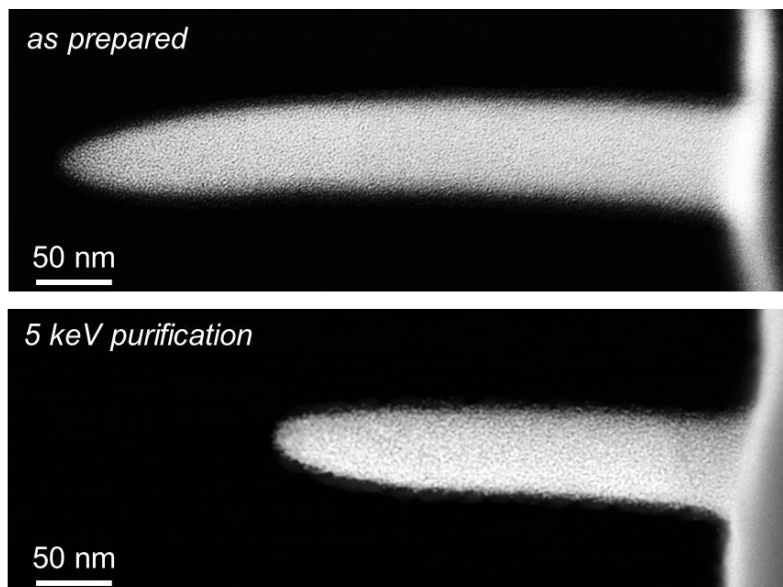

Figure 55: HAADF-TEM images of low aspect ratio nanopillars before (top) and after (bottom) purification. Besides the obvious volume loss the material related contrast increases revealing the loss of carbon.

As a final step, high aspect ratio nanopillars were purified by using the same set of purification parameters as for the low aspect ratio pillars. Figure 57 shows an in-scale comparison of HAADF-TEM images before (left) and after (right) purification. As evident, the pillar contracts laterally by about ~55 % which again is in agreement with theoretical considerations. The much stronger lateral shrinking is only observed for high aspect pillars and can consistently be explained by a spatially isotropic contraction in contrast to flat

deposits which are bounded to the substrate surface. At this point it has to be mentioned that such high aspect pillars tend to be bended during purification as can be seen by the SEM images in Figure 54b. The reason for this effect is most likely local charging of the pillar tip which is then interacting with the scanning electron beam during large area purification scanning. Furthermore, it is assumed that the fast purification process is also contributing to the bending as a result of the small pillar diameters and mechanical stress during purification. Hence, further optimization of the scan routines during purification has to be done in order to prevent lateral bending.
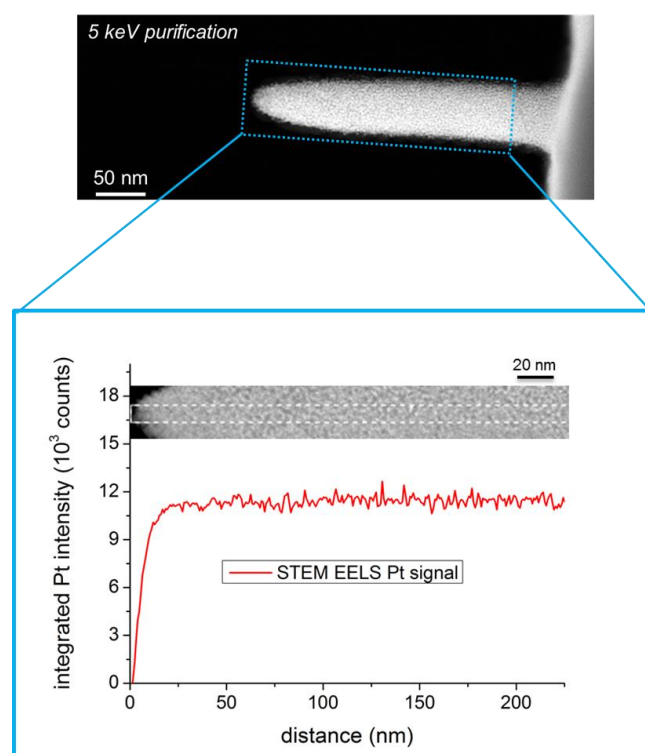

Figure 56: HAADF-TEM image (top) which indicates the area further investigated via STEM-EELS shown in the lower graph revealing a homogeneous Pt signal along the pillar.

Figure 57 also shows increased Pt grains after purification which is elaborated in more details via HR TEM in Figure 58. As can be seen, the single grains are highly crystalline (fringes) and reveal grain sizes in the range of 5 – 6 nm compared to 2 – 3 nm for as-deposited structures. The essence, however, is the fact that beside 3D and quasi-2D structures also free standing quasi-1D architectures can be fully purified with the introduced process making this concept generally applicable for FEBID related metal-matrix (nano-) structures.

Finally, the pillar tips have been investigated on their morphological improvement as can be seen by a direct comparison in Figure 59. As evident, the tip radius is strongly decreased from about 15 nm (left) to less than 5 nm after purification (right) while the Pt grains are slightly increased and closely packed. These findings contain huge potential for AFM related high resolution tips with conductive character as comparable, commercially available products barely provide less than 15 nm tip radius at the moment.

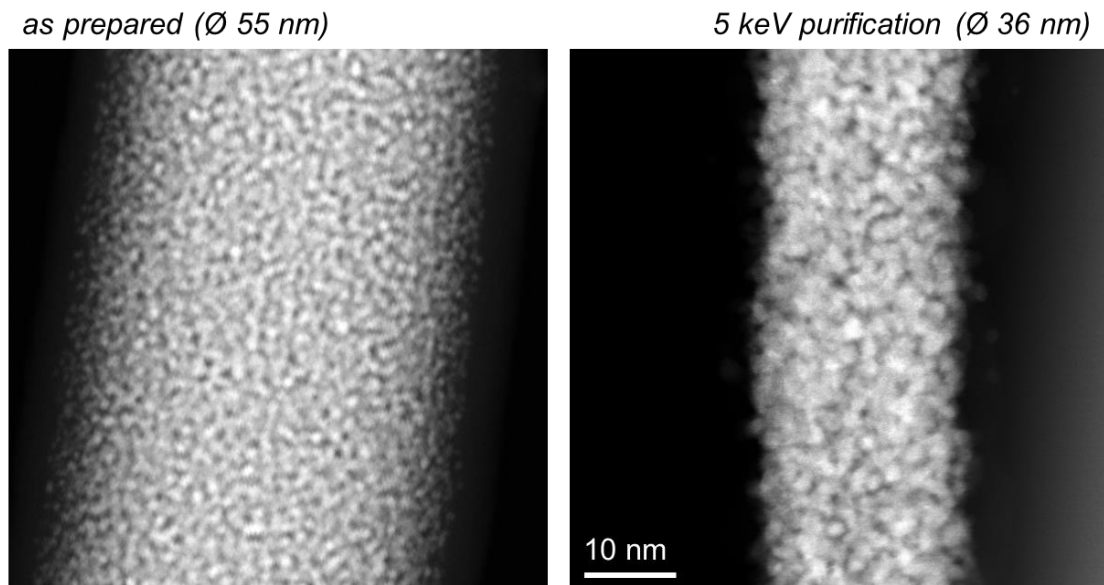*as prepared (Ø 55 nm)*   *5 keV purification (Ø 36 nm)*

Figure 57: HAADF-TEM comparison of high aspect ratio nanopillars before (left) and after (right) purification (both images are in-scale).
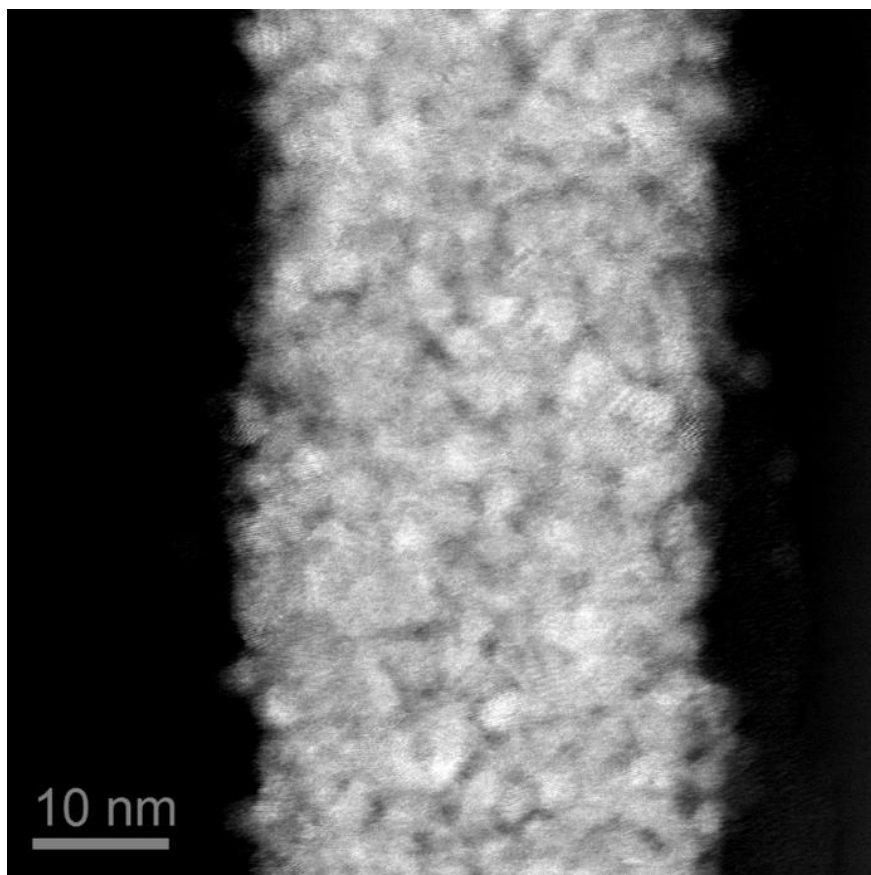

Figure 58: HR-TEM image of a high aspect ratio nanopillar revealing slightly increased but fully crystalline Pt grains.
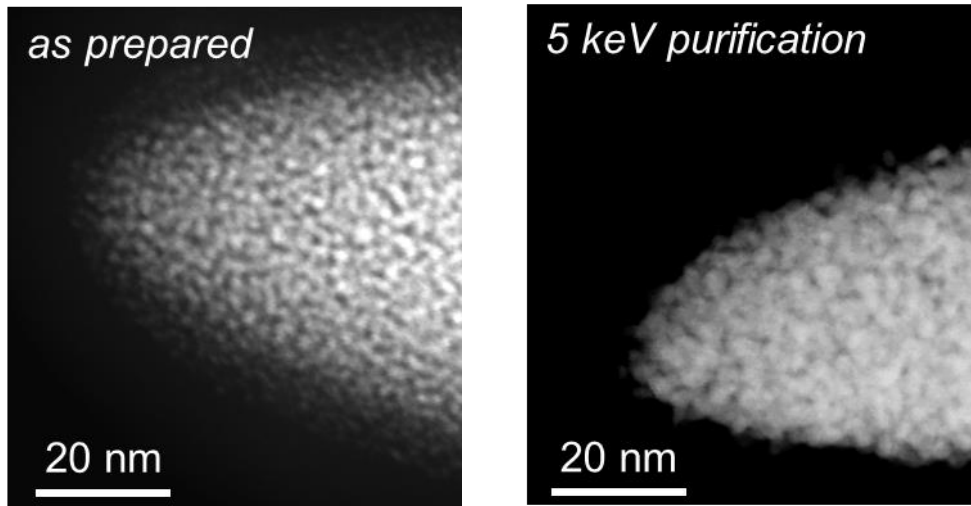
Figure 59: HAADF-TEM images of a nanopillar tip before (left) and after (right) full purification.

4.5 Discussion

All experiments conducted on 3D deposits, discussed in section 4.4.1, reveal that H_2O pressures of 10 Pa are sufficient to establish an electron limited regime (ELR) as much higher pressures of 100 Pa, strongly different DTs and PoPs as well as increased beam currents reveal virtually identical C/Pt ratios and comparable purification efficiencies (see Figure 33).

For a H_2O pressure of 10 Pa an effective H_2O flux Γ_{H_2O} of ~4 x 10^{19} H_2O/(cm².s) and an effective electron flux Γ_e from ~8 x 10^{19} to ~4 x 10^{20} e⁻/(cm².s) was determined which is explained in detail in section 4.3.4. Plank et al.[7] conducted O_2 purification in HV at a local O_2 pressure of ~3 x 10^{-2} Pa and a current density of ~500 A/cm². An O_2 flux Γ_{O_2} of ~1 x 10^{16} O_2/(cm².s) and an electron flux Γ_e of ~3 x 10^{21} e⁻/(cm².s) was calculated. Hence, it is clear that a different regime emerges when the electron flux is similar to the flux of the purification gas as it is the case for the H_2O purification. The total number of carbon atoms in a 70 nm thick PtC_4 deposit with a footprint of 1 cm² is ~4 x 10^{17}, as revealed in section 4.3.4. The total number of electrons needed to purify a 70 nm thick PtC_4 layer (i.e. 30 C.cm⁻²) with a footprint of 1 cm² is ~2 x 10^{20}. Hence, the cumulative efficiency for the electron limited regime is ~0.2 %. Therefore, the experimentally suggested ELR condition is reasonable due to the fact that the equilibrium coverage and the diffusion permeation into the Pt-C structure will be superior in comparison to the O_2 purification.[7] The average diffusion distance of water in several polymer is D = ~1 x 10^{-8} cm²/s, as stated by Métayer et al.[48] Consequently a diffusion distance *d* of 70 nm only takes ~1 ms which is expressed by following relation:[12]

$$t = \frac{d^2}{4D}$$
(9)

These findings strongly suggest that the observed efficiencies show a limitation based on the surface coverage, solubility of water in the platinum carbon structure and it also depends on the electron stimulated cross-section of water on the surface of the deposit and in the carbon matrix.[12]
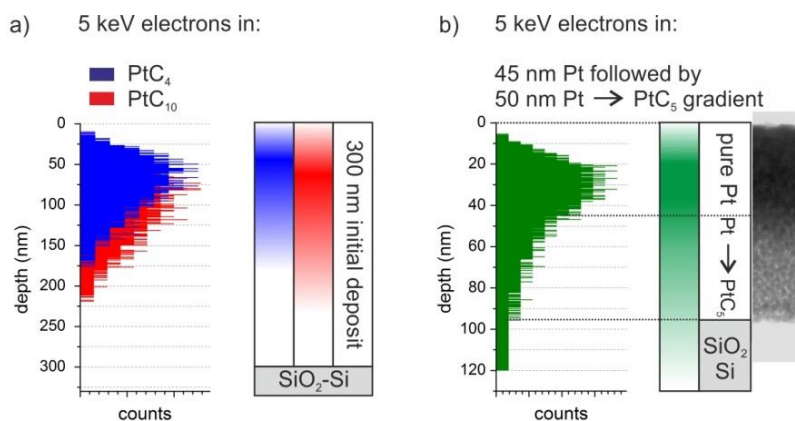

Figure 60: Monte Carlo based simulations of the electron penetration depths assuming different chemistries and layer thicknesses; a) assumes 5 keV electrons in a 300 nm deposit consisting of PtC_4 (blue) and PtC_{10} (red) revealing a maximum penetration depth of less than 230 nm; b) uses the STEM-EELS data from Figure 49 consisting of a 45 nm pure Pt layer on top, followed by 50 nm thick gradient from PtC to PtC_5. As can be seen the reduced thickness together with the varying chemistry lead to full penetration, however, with low spatial electron densities.[12]

The purification was found to be a bottom up process observed via TEM of partially purified deposits (see Figure 44). Together with the observation of limited purification depths two process types are conceivable: *1)* formation of reactive H_2O components on the surface due to interaction with the electron beam further diffusing into the deposit which then reacts in spatial regions according to the electron interaction volume leading to volatile products as e.g. CO, CO_2, CH_x which leave the deposit; and/or *2)* intact H_2O molecules diffuse inside the nanostructure and form radicals according to the electron interaction volume subsequently leading to the formation of the above mentioned volatile species which leave the deposit. For both assumptions, however, the electron interaction volume in the deposit plays an essential role. Therefore, the electron interaction volume in the deposit was simulated with the software CASINO[49] for a wide range of chemical compositions of 9-20 at.% Pt in a carbon matrix ($PtC_{10} \rightarrow PtC_4$) assuming a primary electron energy of 5 keV. Figure 60a reveals the penetration depth of 5 keV electrons in a PtC_4 (blue bars) and PtC_{10} (red bars). It can be seen that the penetration depth of primary electrons is less than 230 nm. Subsequently, for a 300 nm thick deposition, the deepest 80-120 nm (depending on the assumed composition of the carbon matrix) are not reached. However, this is in conflict with the STEM-EELS data where it is obvious that deeper areas are also partly purified as shown in Figure 49. To explain this behavior the high volume loss during purification has to be considered as well. Figure 60b shows the CASINO simulation[30] of the penetration depth of 5 keV electrons according to the STEM-EELS results showing a 45 nm thick pure Pt layer and 50 nm gradient of Pt→PtC_5 (identical to 17 at.% Pt as suggested by EDXS based absolute quantification for the chosen deposition parameters) on top of the SiO_2/Si substrate. Due to the enormous volume loss the electrons finally penetrate the entire layer system and even

reach the substrate. Hence, it is assumed that the 300 nm thick nanostructure can entirely be purified for very long purification times, however, with very low overall efficiencies.[12]
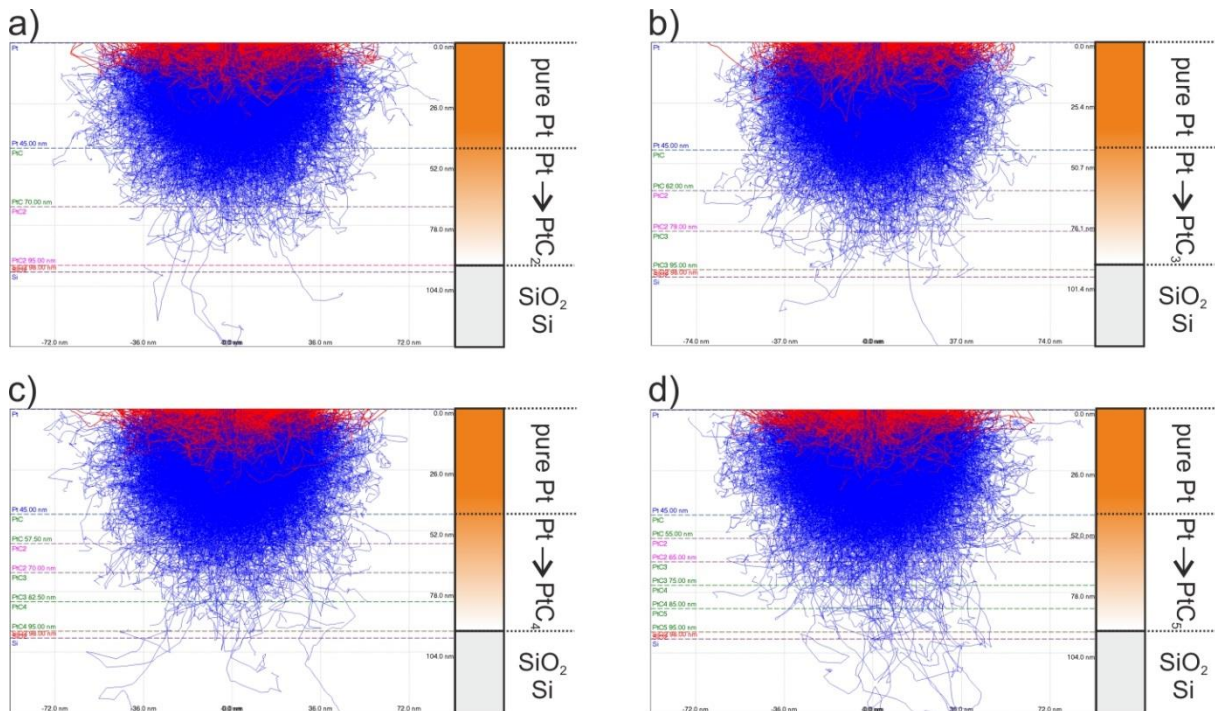

Figure 61: CASINO simulation of 5 keV electron penetration depths in layer stack of 45 nm thick pure Pt on top followed by a 50 nm region with increasing carbon contents: a) Pt→PtC2, b) Pt→PtC3, c) Pt→PtC4 and d) Pt→PtC5. The electrons even reach deepest areas for most dense structures (Pt→PtC2) which explains the partial purification of the initially 300 nm thick deposition even for the deepest areas. Electrons which lose all their energy in the bulk are indicated by the blue trajectories and electrons which left the surface again (BSE) are displayed red.[12]

To complete these considerations, further CASINO simulations[30] were done with varying chemistries of the 50 nm thick, partially purified layer underneath the 45 nm thick Pt layer on top. In more detail, the gradient was systematically changed from Pt→PtC to Pt→PtC$_5$ as summarized in Figure 61. From this finding it can be seen that even for the densest structure of Pt→PtC$_2$ primary electrons reach the deepest areas of the deposit which explains the partial purification of the nanostructure as observed via STEM-EELS results in Figure 49. This is consistent with that the initially 150 nm thick deposit is completely purified resulting in a 49 nm dense layer. This suggests that for purification of thick samples, either the electron energy has to be increased, which results in larger electron interaction volumes, or – if possible - the deposit thickness has to be adapted according to the possible purification energy.

These findings also explain the significant increase of the minimal purification time of the initially 165 nm thick deposition (see Figure 37). It is expected that the purification process starts in volumes similar to the interaction volume of 5 keV electrons in PtC$_4$ (see Figure 60). As the purification process is very fast the spatial chemistry distribution changes together with vertical shrinking which leads also to a densification of the structure and a shift of the electron interaction volume to deeper areas. As the electron interaction volume decreases

significantly for deeper regions in a 165 nm high structure the efficiency of the purification process decreases enormously as mentioned above and illustrated in Figure 37.
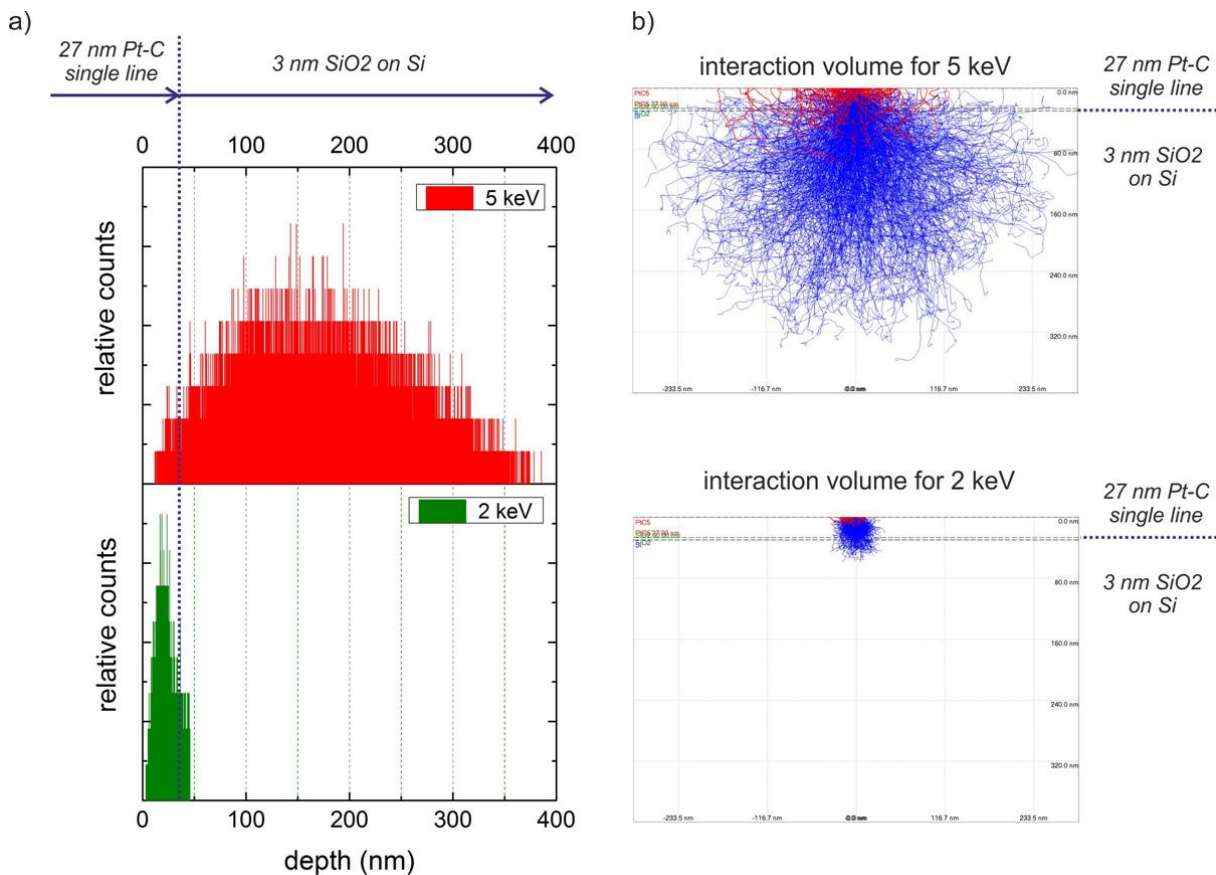

Figure 62: CASINO simulations of 5 keV and 2 keV electrons in 27 nm thick single lines deposited on SiO₂/Si substrates. While a) gives the respective penetration depths of electrons, b) shows the interaction volume on same scales for 5 keV and 2 keV, respectively.

Experiments conducted on quasi-2D single lines (see section 4.4.2) suggest that the efficiency of the purification process also depends on the spatial electron densities. This was reflected by the observation that low purification currents only led to 13 % height loss while high currents lead to more than 55 %. As comparison, purification of $2 \times 2\ \mu m^2$ nanostructures at low currents also revealed slightly lower volume losses although STEM-EELS analyses confirmed entire carbon removal. We attribute this behavior to different grain growth characteristics revealing smaller crystals for higher currents. This assumption is also in agreement with the observation that fully purified lines with less than 4 nm thickness were found which would also limit the maximum grain size to these dimensions. Although beyond the scope of this thesis, further experiments on electron-density to grain-size relations are needed to clarify this assumption indirectly derived from experimental observations. Finally, Monte Carlo simulations have been conducted for 27 nm thick single lines on SiO₂/Si assuming different primary energies. As can be seen in Figure 62b the interaction volume for 5 keV electrons reach deep into the substrate also reflected by the according depth distribution (red bars). This distribution has strong effects on the spatial SE density in the material which is comparable low as many SE electrons are generated in the substrate. Changing the primary electrons to e.g. 2 keV massively improves the situation as can be

seen by the related interaction volume and electron depth distributions shown in Figure 62, respectively. Most of the electrons stay within the single lines themselves and lead to maximum spatial SE densities within the deposit. Furthermore, as can be seen by a direct comparison of the primary electron energy distribution in Figure 63 for 2 keV (a) and 5 keV (b) most of the low energy electrons lose their energy within the deposit, hence, also contributing to the purification process. These simulations visualize the above mentioned demand for adapted primary energies to the deposit thickness (or vice versa if possible) to maximize both efficiencies as well as passing the postulated threshold to initiate the purification experiments (see discussion in section 4.4.2 on single lines).
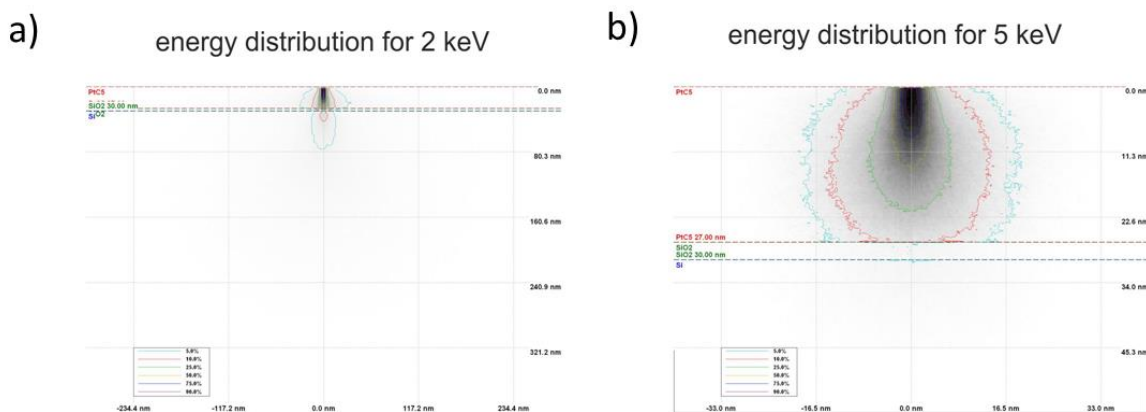

Figure 63: energy distribution for 2 keV a) and 5 keV electrons b).

Finally, quasi-1D nanopillars were purified by a H_2O pressure of 100 Pa primarily intended to compensate for lower surface diffusion compared to quasi-2D single lines and 3D structures. 2 x 2 μm^2 nanostructures as nanopillars reveal enormous aspect ratios which can entirely shut down substrate related replenishment contributions. The results, however, revealed another effect of the high pressures used as the skirt effect related scattering factor is estimated to ~50 % (for electrons traveling through a H_2O vapour at 100 Pa by a WD of 11 nm). This leads to the situation that the potentially purifying electrons are not entering the nanopillars from top but also at the side walls by scattered contributions. This allows purification of even high, free-standing structures making this approach very powerful for 3D architectures. TEM investigations again revealed slight Pt grain growth from 2-3 nm to 5-6 nm and an according volume loss of up to 55 % (see section 4.4.3) in agreement with theoretical consideration concerning the full removal of carbon. At this point it should be mentioned again that although unwanted pillar bending was observed during purification, alternative scanning routines have the potential to compensate for this effect (e.g. spiral scanning or spot exposure with a defocused beam), however, this might limit the influence of the scattered electrons in the gas on the purification process.

Although not all possible parameters have been varied (see introduction Figure 25) the presented data represent consistent proof-of-concept of the introduced purification approach using an e-beam assisted H_2O purification method at room temperature. The entire set of data allowed furthermore a comprehensive functional insight from a fundamental point of view allowing predictions for the remaining parameters.

5 Summary and Outlook

The main result of this master thesis is the introduction of a simple and rapid approach for entire carbon removal from $MeCpPt^{IV}Me_3$ based FEBID (nano)structures resulting in pore free, high fidelity deposits. The thesis confirmed furthermore the applicability for 3D, quasi-2D (single lines) and quasi-1D (nanopillars) structures making this approach highly interesting for new nano-applications to be developed at the FELMI.

In more detail, FEBID structures were initially fabricated with a wide range of process parameters and subsequently purified in an environmental scanning electron microscope (ESEM) allowing for spatially homogeneous and controlled H_2O partial pressures at room temperature. The final structures were morphologically, structurally and chemically characterized via scanning electron microscopy (SEM), atomic force microscopy (AFM) and transmission electron microscopy (TEM) for a comprehensive insight.

First, the influence of H_2O chamber pressures on purification efficiencies and purities have been investigated revealing similar results for lowest (10 Pa) and highest (100 Pa) possible chamber pressures. Next, the influence of the deposition regime on the purification process was elaborated by fabricating FEBID structures in electron and molecule limited regime conditions as they lead to different carbon types in the matrices. Again identical results were found in terms of efficiency and degree of purity. Finally, systematic variation of purification parameters by means of pixel dwell time, pixel distance, beam currents and chamber pressure revealed a wide independency suggesting electron limited regime conditions during purification even for lowest H_2O pressures of 10 Pa at rates better than 5 $min.nA^{-1}.\mu m^{-2}$ corresponding to a dose of 30 $C.cm^{-2}$.

Morphological characterization via AFM revealed a volume loss of (69 ± 3) vol.% for all deposits which is in accordance with the theoretically predicted value of 70 vol.%. One of the main achievements of this thesis, however, is the fact that the introduced purification approach led to *1)* pore- and crack-free deposits after full purification while the original footprint shape was entirely maintained with a minimal shrink of less than 4 %. Even pseudo 3D surface features were widely unaffected by the purification process making this approach highly interesting for even more complex 3D architectures.

Chemical characterization via TEM based methods finally confirmed the entire removal of carbon for initial deposit heights of 150 nm by using 5 keV primary energies during purification. Furthermore, the Pt grains have been found to grow from typical 2-3 nm to 6-9 nm. Finally, TEM analyses could identify the purification as a bottom-up process which suggests the mechanism to an inwards diffusion of either dissociated or non-dissociated water molecules which are then reacting in the presence of low-energy electrons according to the interaction volume. The volatile CO_2, CO or CH_x products are then assumed to diffuse outwards through the less dense carbon matrix on top or along grain boundaries allowing Pt grains to rearrange perfectly.

After these proof-of-concept studies the deposit dimensionality was reduced to quasi-2D and quasi-1D by means of FEBID single lines and free standing nanopillars, respectively. For single lines vertical volume losses in the range of 55 % could be demonstrated with minimal shrinking of the single line base widths. Although no pores and/or cracks were found,

thinnest lines (4.5 nm after purification) reveal a slight roughness increase from 0.5 nm to about 1.3 nm (RMS). Dedicated current and time studies, however, suggested that a certain spatial electron density is required to obtain highest purification performance by means of purity. Complementary Monte Carlo simulation supported this assumption as for such small volumes only a minor fraction of incoming electrons contribute directly or indirectly (via secondary electrons) to the purification process.

Finally, free-standing nanopillars were successfully subjected to the introduced purification approach. It was found that depending on the pillar height the structure shrinks preferably vertically (low aspect ratios) or laterally (high aspect ratios) which suggests a basically isotropic shrinking, however, influenced by mechanical constraints with respect to the substrate bonding. The pillar tips also reduced their tip radius making this architecture in combination with the purification process highly promising for nanoscale applications due to their simple and fast fabrication and post-growth-treatment.

Thus, the introduced purification approach has been proven to be applicable for different dimensionalities leading to highly pure Pt structures while original shapes are maintained without the formation of pores and/or cracks. The fact that the process is electron limited in ESEM conditions makes this approach furthermore simple to set up and almost straightforward in application as no complicated process adaption has to be done. Finally, as no highly reactive gases and/or elevated temperatures are used, this approach does not limit the application with respect to sensitive substrate materials.

As the results of this thesis represent the first route towards such high quality Pt deposits based on FEBID structures new applications such as free standing quasi-1D resonators, sensors and even plasmonics are conceivable which are currently under development at the Institute for Electron Microscopy at the Graz University of Technology.

References

1. Utke I, Russel PE. *Nanofabrication using focused ion and electron beams: Principles and applications.* 1st ed. New York: Oxford University Press; 2012:840.

2. Perentes A, Bachmann A, Leutenegger M, Utke I, Sandu C, Hoffmann P. Focused electron beam induced deposition of a periodic transparent nano-optic pattern. *Microelectron Eng.* 2004;73-74:412-416.

3. Kolb F, Schmoltner K, Huth M, et al. Variable tunneling barriers in FEBID based PtC metal-matrix nanocomposites as a transducing element for humidity sensing. *Nanotechnology.* 2013;24(30).

4. Plank H, Gspan C, Dienstleder M, Kothleitner G, Hofer F. The influence of beam defocus on volume
growth rates for electron beam induced
platinum deposition. *Nano.* 2008;19:485302-1-485302-9.

5. Plank H, Kothleitner G, Hofer F, et al. Optimization of postgrowth electron-beam curing for focused electron-beam-induced pt deposits. *J Vac Sci Technol B Microelectron Nanometer Struct.* 2011;29(5).

6. Plank H, Smith DA, Haber T, Rack PD, Hofer F. Fundamental proximity effects in focused electron beam induced deposition. *ACS Nano.* 2012;6(1):286-294.

7. Plank H, Noh JH, Fowlkes JD, Lester K, Lewis BB, Rack PD. Electron-beam-assisted oxygen purification at low temperatures for electron-beam-induced pt deposits: Towards pure and high-fidelity nanostructures. *ACS Applied Materials and Interfaces.* 2014;6(2):1018-1024.

8. Plank H, Haber T, Gspan C, Kothleitner G, Hofer F. Chemical tuning of PtC nanostructures fabricated via focused electron beam induced deposition. *Nanotechnology.* 2013;24(17).

9. Winkler R, Fowlkes J, Szkudlarek A, Utke I, Rack PD, Plank H. The nanoscale implications of a molecular gas beam during electron beam induced deposition. *ACS Appl Mater Interfaces.* 2014;6(4):2987-2995.

10. Arnold G, Timilsina R, Fowlkes J, Orthacker A, Kothleitner G, Rack P.D.,Plank H, Fundamental resolution limitations during electron induced direct write synthesis. *ACS Applied Materials and Interfaces.* 2014;6(10):7380-7.

11. Winkler R, Geier B, Plank H, Spatial chemistry evolution during focused electron beam induced depositions: Origins and workarounds. *Applied physics A.* 2014;in press.

12. Geier B, Gspan C, Winkler R, Schmied R, Fowlkes J.D, Fitzek H, Rauch S, Rattenberger J, Rack P.D., Plank H, Rapid and highly compact purification for focused electron beam induced depositis: A low temperature approach using electron stimulated H_2O reactions. *Journal of Physical Chemistry C.* 2014; DOI: 10.1021/jp503442b.

13. Huth M, Kolb F, Plank H, Dielectric sensing by charging energy modulation in nanogranular metal. *Applied physics A.* 2014;in press.

14. Mulders JJL, Belova LM, Riazanova A. Electron beam induced deposition at elevated temperatures: Compositional changes and purity improvement. *Nanotechnology.* 2011;22(5).

15. Randolph SJ, Fowlkes JD, Rack PD. Focused, nanoscale electron-beam-induced deposition and etching. *Crit Rev Solid Statae Mater Sci.* 2006;31(3):55-89.

16. Roberts NA, Fowlkes JD, Magel GA, Rack PD. Enhanced material purity and resolution via synchronized laser assisted electron beam induced deposition of platinum. *Nanoscale.* 2013;5(1):408-415.

17. Roberts NA, Magel GA, Hartfield CD, Moore TM, Fowlkes JD, Rack PD. In situ laser processing in a scanning electron microscope. *Journal of Vacuum Science and Technology A: Vacuum, Surfaces and Films.* 2012;30(4).

18. Gopal V, Stach EA, Radmilovic VR. Metal delocalization and surface decoration in direct-write nanolithography
by electron beam induced deposition. *App Phys Lett.* 2004;85(1):49-51.

19. Botman A, Mulders JJL, Weemaes R, Mentink S. Purification of platinum and gold structures after electron-beam-induced deposition. *Nanotechnology.* 2006;17(15):3779-3785.

20. Langford RM, Wang T-, Ozkaya D. Reducing the resistivity of electron and ion beam assisted deposited pt. *Microelectronic Engineering.* 2007;84(5-8):784-788.

21. Mehendale S, Mulders JJL, Trompenaars PHF. A new sequential EBID process for the creation of pure pt structures from MeCpPtMe3. *Nanotechnology.* 2013;24(14).

22. Langford RM, Ozkaya D, Sheridan J, Chater R. Effects of water vapour on electron and ion beam deposited platinum. *Microsc Microanal.* 2004;10(SUPPL. 2):1122-1123.

23. Gopal V, Radmilovic VR, Daraio C, Jin S, Yang P, Stach EA. Rapid prototyping of site-specific nanocontacts by electron and ion beam assisted direct-write nanolithography. *Nano Lett.* 2004;4(11):2059-2063.

24. Porrati F, Sachser R, Schwalb CH, Frangakis AS, Huth M. Tuning the electrical conductivity of pt-containing granular metals by postgrowth electron irradiation. *J Appl Phys.* 2011;109(6).

25. Frabboni S, Gazzadi GC, Felisari L, Spessot A. Fabrication by electron beam induced deposition and transmission electron microscopic characterization of sub- 10-nm freestanding pt nanowires. *Appl Phys Lett.* 2006;88(21).

26. Botman A, Mulders JJL, Hagen CW. Creating pure nanostructures from electron-beam-induced deposition using purification techniques: A technology perspective. *Nanotechnology.* 2009;20(37).

27. Courtesy of DI Robert Winkler, Institute for Electron Microscopy and Nanoanalysis, Graz University of Technology, Austria, 2014.

28. Goldstein J, Newbury D, Joy DC, et al. *Scanning electron microscopy and X-ray microanalysis.* 3rd Edition ed. New York: Springer Scienes+Business Media, Inc.; 2003.

29. The FEI Company. Manual FIB Nova 200. Eindhoven, The Netherlands, www.fei.com.

30. Drouin D, Couture AR, Joly D, Tastet X, Aimez V, Gauvin R. CASINO V2.42 - A fast and easy-to-use modeling tool for scanning electron microscopy and microanalysis users. *Scanning.* 2007;29(3):92-101.

31. Reimer L. *Scanning electron microscopy: Physics of image formation and microanalysis.* Vol 45. 2 completely rev a updat ed. Berlin ; New York: Springer; 1998:527. http://www.loc.gov/catdir/enhancements/fy0812/98026178-d.html.

32. Courtesy of Dr. Harald Plank, Institute for Electron Microscopy and Nanoanalysis, Graz University of Technology, Austria, 2014.

33. Robert Johnson, ed. *Environmental scanning electron microscopy - an introdcution to ESEM.* 2nd ed. ; 1996. Philips Electron Optics, ed.

34. Danilatos GD, ed. *Foundations of environmental scanning electron microscopy.* ; 1988Advances in Electronics and Electron Physics; No. 71.

35. Thiel BL. Master curves for gas amplification in low vacuum and environmental scanning electron microscopy. *Ultramicroscopy.* 2004;99(1):35-47.

36. Fletcher AL, Thiel BL, Donald AM. Amplification measurements of alternative imaging gases in environmental SEM. *J Phys D.* 1997;30(15):2249-2257.

37. Master Thesis by Harald Fitzek, Institute for Electron Microscopy, Graz University of Technology, 2014.

38. Rattenberger J, Wagner J, Schröttner H, Mitsche S, Zankel A. A method to measure the total scattering cross section and effective beam gas path length in a low-vacuum SEM. *Scanning.* 2009;31(3):107-113.

39. Courtesy of Ao.-Univ.-Prof. Dipl.-Ing. Dr. techn. Werner Grogger, Institute for Electron Microscopy and Nanoanalysis, Graz University of Technology, Austria, 2014.

40. Williams DB, Carter CB. Transmission electron microscopy: A textbook for materials science. *Transmission Electron Microscopy: A Textbook for Materials Science.* 2009:1-760.

41. Engmann S, Stano M, Papp P, Brunger MJ, Matejcík Š, Ingólfsson O. Absolute cross sections for dissociative electron attachment and dissociative ionization of cobalt tricarbonyl nitrosyl in the energy range from 0 eV to 140 eV. *J Chem Phys.* 2013;138(4).

42. Winkler R, Fowlkes J, Szkudlarek A, Utke I, Rack PD, Plank H. The nanoscale implications of a molecular gas beam during electron beam induced deposition. *ACS Applied Materials and Interfaces.* 2014;6(4):2987-2995.

43. Master Thesis by DI Robert Winkler, Center for Electron Microscopy, Graz University of Technology, 2014.

44. Winkler R, Fowlkes J, Szkudlarek A, Utke I, Rack PD, Plank H. The nanoscale implications of a molecular gas beam during electron beam induced deposition. *ACS Applied Materials and Interfaces.* 2014;6(4):2987-2995.

45. Rattenberger J, Wagner J, Schröttner H, Mitsche S, Zankel A. A method to measure the total scattering cross section and effective beam gas path length in a low-vacuum SEM. *Scanning*. 2009;31(3):107-113.

46. Danilatos G, Rattenberger J, Dracopoulos V. Beam transfer characteristics of a commercial environmental SEM and a low vacuum SEM. *J Microsc*. 2011;242(2):166-180.

47. Dracopoulos V, Danilatos G. ESEM modifications to LEO SUPRA 35 VP FESEM. *Micron*. 2013;44(1):238-245.

48. Métayer M, Labbé M, Marais S, et al. Diffusion of water through various polymer films: A new high performance method of characterization. *Polym Test*. 1999;18(7):533-549.

49. Drouin D, Couture AR, Joly D, Tastet X, Aimez V, Gauvin R. CASINO V2.42 - A fast and easy-to-use modeling tool for scanning electron microscopy and microanalysis users. *Scanning*. 2007;29:92-101.